BAMS Article

CROSSINN

A Field Experiment to Study the Three-Dimensional Flow Structure in the Inn Valley, Austria

Bianca Adler, Alexander Gohm, Norbert Kalthoff, Nevio Babić, Ulrich Corsmeier, Manuela Lehner, Mathias W. Rotach, Maren Haid, Piet Markmann, Eckhard Gast, George Tsaknakis, and George Georgoussis

ABSTRACT: While the exchange of mass, momentum, moisture, and energy over horizontally homogeneous, flat terrain is mostly driven by vertical turbulent mixing, thermally and dynamically driven mesoscale flows substantially contribute to the Earth–atmosphere exchange in the atmospheric boundary layer over mountainous terrain (MoBL). The interaction of these processes acting on multiple scales leads to a large spatial variability in the MoBL, whose observational detection requires comprehensive instrumentation and a sophisticated measurement strategy. We designed a field campaign that targets the three-dimensional flow structure and its impact on the MoBL in a major Alpine valley. Taking advantage of an existing network of surface flux towers and remote sensing instrumentation in the Inn Valley, Austria, we added a set of ground-based remote sensing instruments, consisting of Doppler lidars, a ceilometer, a Raman lidar, and a microwave radiometer, and performed radio soundings and aircraft measurements. The objective of the Cross-Valley Flow in the Inn Valley Investigated by Dual-Doppler Lidar Measurements (CROSSINN) experiment is to determine the mean and turbulent characteristics of the flow in the MoBL under different synoptic conditions and to provide an intensive dataset for the future validation of mesoscale and large-eddy simulations. A particular challenge is capturing the two-dimensional kinematic flow in a vertical plane across the whole valley using coplanar synchronized Doppler lidar scans, which allows the detection of cross-valley circulation cells. This article outlines the scientific objectives, instrument setup, measurement strategy, and available data; summarizes the synoptic conditions during the measurement period of 2.5 months; and presents first results.

Keywords: Boundary layer; Valley/mountain flows; Atmosphere-land interaction; Aircraft observations; Lidars/Lidar observations; Remote sensing

https://doi.org/10.1175/BAMS-D-19-0283.1

Corresponding author: Bianca Adler, bianca.adler@noaa.gov

In final form 19 August 2020

AFFILIATIONS: Adler,* Kalthoff, Babić, and Corsmeier—Karlsruhe Institute of Technology, Karlsruhe, Germany; **Gohm, Lehner, Rotach, and Haid**—University of Innsbruck, Innsbruck, Austria; **Markmann and Gast**—METEX GmbH, Elmshorn, Germany; **Tsaknakis and Georgoussis**—Raymetrics S.A., Athens, Greece
*** Current affiliation:** CIRES, University of Colorado Boulder, and NOAA/Physical Sciences Laboratory, Boulder, Colorado

The atmospheric boundary layer over mountainous terrain (MoBL) is highly variable in space and time (e.g., Rotach and Zardi 2007). This is because the exchange of mass, momentum, moisture, and energy is affected by processes spanning a large range of scales from millimeters to kilometers (e.g., Lehner and Rotach 2018). Vertical and horizontal turbulent mixing related to buoyancy or shear (e.g., Strauss et al. 2016; Serafin et al. 2018), thermally driven flows such as slope and valley winds (e.g., Zardi and Whiteman 2013), dynamically driven flows like gravity waves and foehn (e.g., Jackson et al. 2013; Serafin et al. 2017), and moist orographic convection (e.g., Kirshbaum et al. 2018) all impact the exchange and the conditions in the MoBL. In particular in valleys and basins, the exchange is relevant for the dispersion of air pollutants and thus for the air quality (e.g., Steyn et al. 2013; Karl et al. 2020). Idealized simulations indicate that the transport from the surface to the free atmosphere may be 3–4 times more effective over valleys than over flat terrain—depending on the valley geometry and atmospheric conditions (e.g., Wagner et al. 2015; Leukauf et al. 2017). Since a large part of the land surface consists of mountainous terrain, the MoBL plays an essential role in the total exchange between the Earth and the atmosphere (Rotach et al. 2014). Thus, an accurate understanding of the relevant processes is crucial to a correct representation of the exchange in numerical weather prediction and global and climate models. Although the MoBL has been investigated for several decades, the understanding of transport and exchange processes remains still to be improved (e.g., Lehner and Rotach 2018). One reason for this is the challenge to capture the decisive processes and structures experimentally, as the large range of involved scales requires continuous area wide measurements with appropriate high spatial and temporal resolution.

In valleys, the superposition of the various processes leads to a complex vertical layering in the MoBL (e.g., De Wekker and Kossmann 2015). When thermally driven flows are dominant, a three-layer thermal structure consisting of a lower and upper well-mixed layer separated by an inversion (called "stable valley atmosphere"; Lehner and Rotach 2018) is often reported. Analytical theory and idealized numerical simulations suggest that this structure is related to two vertically stacked circulation cells that form due to partial redirection of the upslope flow toward the valley center when stability increases with height (e.g., Vergeiner 1982; Vergeiner and Dreiseitl 1987; Schmidli 2013; Wagner et al. 2015). While numerical (e.g., Serafin and Zardi 2010; Goger et al. 2019) and observational (Adler and Kalthoff 2014) evidence of enhanced turbulence in the upper well-mixed layer has been reported, there is no direct experimental detection of the stacked circulation cells so far. The number of observational studies which investigate the spatial structure of the flow in valleys is limited: for cases when the cross-valley component of the large-scale wind is strong, scanning ground-based remote sensing instruments such as Doppler lidars partly in combination with research aircraft measurements have successfully been used to study rotors (e.g., Hill et al. 2010; Strauss et al. 2016), downslope windstorms (e.g., Adler and Kalthoff 2016), and foehn events (e.g., Haid et al. 2020). For periods when thermally driven flows and convection dominate the conditions in the valley, observations of the spatial structure in the MoBL above the surface layer are mostly based on research aircraft flights and radio soundings during meteorological field campaigns (e.g., Weigel and Rotach 2004), which can only provide snapshot information. The fact that continuous area-wide measurements of the flow field in valleys under different large-scale conditions are still rare motivated the Cross-Valley Flow in the Inn Valley Investigated by Dual-Doppler Lidar

Measurements (CROSSINN) project. The addressed research questions, which are formulated in Table 1, can roughly be divided into three categories: (i) the kinematic flow structure in the valley, (ii) the impact of the flow in the valley on the MoBL characteristics, and (iii) the influence of the synoptic scale flow and surface conditions on the flow structure in the valley.

We chose the Inn Valley in Austria—a major valley in the Tyrolean Alps—as the target area for the CROSSINN meteorological field campaign for several reasons: from the scientific point of view, the Inn Valley is well suited. Previous observational and numerical studies (overviewed in the next section) revealed that not only a typical MoBL with thermally driven valley and slope winds and a multilayered vertical structure form here, but also dynamically driven processes, e.g., foehn, occur. In addition, tributaries and a slightly curved valley axis allow us to study to what extent the results from idealized numerical simulations, e.g., symmetric cross-valley circulations, hold for a real-world valley. With a maximum ridge-to-ridge distance of less than 20 km, the valley is narrow enough to be captured with ground-based remote sensing, but wide enough to be probed with a research aircraft in cross-valley direction, too. From the practical point of view, it comes with a well-developed infrastructure and an existing network of flux towers and remote sensing instruments. The research questions (Table 1) and the high demands made on the experimental recording which arise from the challenge to capture the spatial variability of the flow guided the planning of this field campaign and governed the choice of instrumentation and measurement strategy. This article provides an overview of the 2.5-month-long CROSSINN field campaign, which was conducted from July to October 2019, and presents some initial results highlighting how the complementary in situ and remote sensing instruments can be used to obtain the most complete picture to date of the atmospheric conditions and processes in the Inn Valley.

MoBL research in the Inn Valley

Research of the MoBL in the Inn Valley started a long time ago. Based on measurements conducted during the Slope Wind Experiment in Innsbruck in 1978, Brehm (1982) and Brehm and Freytag (1982) studied the erosion of the nocturnal inversion by subsidence and convection. In 1982, the Mesoscale Experiment in the Region Kufstein–Rosenheim (MERKUR) experiment was performed in connection with the Alpine Experiment (ALPEX; Kuettner and O'Neill 1981) and investigated the mass and energy budget in the lower part of the valley (Freytag 1985, 1987). Vergeiner and Dreiseitl (1987) described the slope and valley winds in detail and also gave the first estimation of the average monthly onset and end times of the upvalley wind. Zängl (2004, 2009) performed numerical simulations to assess the impact of tributaries on the valley wind and its dependence on the large-scale flow. The Inn Valley and one of its tributaries, the Wipp Valley, were one of the target areas of the Mesoscale Alpine Program (MAP; Bougeault et al. 2001) in 1999, during which foehn and gap flows (e.g., Gohm et al. 2004) as well as thermally driven valley winds (e.g., Rucker et al. 2008) were investigated. Episodes with high air pollution were investigated in winter 2005/06 during the field campaign of the Monitoring and Minimisation of Traffic-Induced Noise and

Table 1. Selected research questions.

Flow structure	What is the spatial structure of the kinematic flow across the Inn Valley? How variable is the flow structure in along-valley direction? What is the relationship between the cross- and along-valley flow? What is the impact of tributary valleys on the flow?
Impact of the flow on the MoBL	How do the vertical thermodynamic structure and the mean and turbulent characteristics of the MoBL depend on the three-dimensional kinematic flow structure in the valley? How do the processes occurring in the valley affect the applicability of different standard methods to determine the MoBL depth, e.g., based on radiosonde or Doppler lidar profiles?
Synoptic scale and surface impacts on the flow	How does the flow in the Inn Valley depend on the large-scale conditions, atmospheric stratification, and surface energy exchange? How does foehn interact with the thermally driven cross- and along-valley circulations?

Air Pollution along Major Alpine Transport Routes (ALPNAP) project (e.g., Gohm et al. 2009; Harnisch et al. 2009; Schnitzhofer et al. 2009). During the recent Penetration and Interruption of Alpine Foehn (PIANO) field campaign in 2017, the processes controlling the penetration of foehn over Innsbruck were studied (Haid et al. 2020; Muschinski et al. 2021). Since around 2013, long-term measurements have been conducted at several sites with the Innsbruck box (i-Box; Rotach et al. 2017). The data were, for example, used to assess the challenges of turbulence measurement over mountainous terrain (Stiperski and Rotach 2016), to develop an objective method to identify ideal valley-wind days (Lehner et al. 2019), to investigate the properties of similarity scaling (Sfyri et al. 2018) and the isotropy characteristics of turbulence (Stiperski et al. 2019) over complex terrain, and to evaluate different turbulence parameterization schemes in numerical models (Goger et al. 2018, 2019). All these activities and campaigns provided a lot of insight in the MoBL structures and processes happening in the Inn Valley. However, in particular the earlier campaigns, which focused on the thermally driven flows, were mainly based on in situ profile measurements and thus lacked information on the three-dimensional structure and variability of the flow. This issue can nowadays be addressed by using state-of-the-art remote sensing technology.

Field campaign design

The CROSSINN field campaign ran from 1 August until 13 October 2019, while the deployment of the instrumentation already started in July. The campaign took place in the area of the i-Box surface flux towers (Rotach et al. 2017) in the lower part of the Inn Valley in Austria, about 20 km east of the city of Innsbruck (Fig. 1). The Inn Valley is a major valley in the Tyrolean Alps, which is approximately southwest-to-northeast oriented in the area east of Innsbruck. In the investigation area, the valley axis is slightly curved to the right when looking in upvalley direction. The tree line is around 1,900 m above mean sea level (MSL) and the valley floor and lower part of the slopes are characterized by mixed agricultural land and villages. The valley floor is about 2–3 km wide and the ridge-to-ridge distance is less than 20 km. In the investigation area, the terrain elevation ranges from around 500 m MSL at the valley floor up to around 2,700 m MSL at the mountain ridges to the south and north of the valley. A mean ridge height of 1,630 m MSL is defined as the mean of all pixels (10 m × 10 m) in the investigation area (Fig. 1b) where the terrain height is larger than the 75th percentile. While the steep slopes to the north are rather uniform with no major side valleys, several tributaries enter the Inn Valley from the south. In the inside bend of the valley north of Kolsass, a plateau at about 850 m MSL extends over several kilometers.

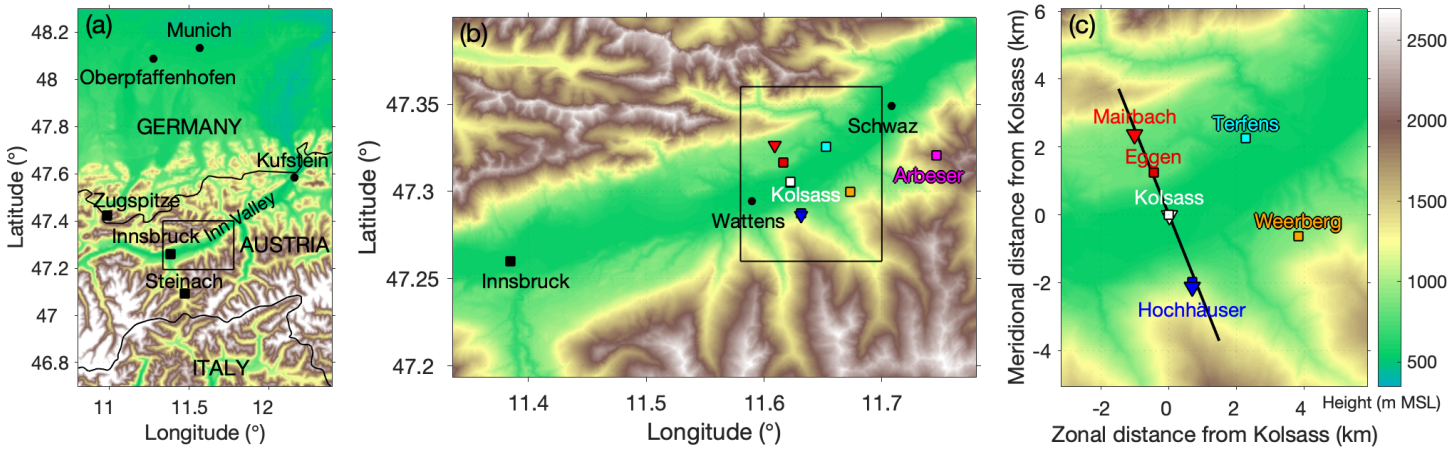

Fig. 1. Orographic map of (a) the Tyrolean Alps, (b) the investigation area in the lower Inn Valley, and (c) close-up of the orographic map of the investigation area. Markers indicate the locations of towns (circles), automatic weather stations (black squares), i-Box surface flux towers (colored squares), and the three Windcube 200s lidars (triangles).

The field campaign was designed to continuously monitor the flow in the Inn Valley and the thermodynamic properties of the MoBL. To this purpose, we expanded the existing network of the six i-Box flux towers and remote sensing instruments by additional remote sensing and in situ instruments to measure wind, temperature, and humidity (Table 2 and Figs. 1c and 2). The setup was optimized to capture the two-dimensional cross-valley flow and the vertical MoBL structure in the valley center, but additional information on the along-valley variability was obtained by aircraft measurements. Three scanning Doppler lidars (Windcube 200s) at Mairbach, Kolsass, and Hochhäuser performed synchronized coplanar range–height indicator (RHI) scans to continuously record the cross-valley circulation in a vertical plane across the Inn Valley. Profiles of the horizontal wind were continuously monitored by another Doppler lidar (Streamline) at Kolsass. Information on the turbulent structure of the MoBL and horizontal variability of the flow was obtained from a fifth Doppler lidar [Streamline eXtended Range (XR)] that performed a combination of vertical stare and plan position indicator (PPI) scans. To close the vertical gap in wind measurements between the i-Box flux tower at Kolsass and the lowest measurement height of the Doppler lidars, a sixth lidar (Wind Ranger) was operated which started measuring less than 10 m above the ground. To continuously monitor the thermodynamic MoBL characteristics, a Raman temperature lidar and microwave radiometers were deployed to record temperature and humidity profiles and a ceilometer detected the backscatter layering and clouds in the valley. Based on the daily issued weather forecast, we identified days with suitable fair weather conditions, as clouds and precipitation strongly limit the performance of the remote sensing instruments and prevent visual flights with the aircraft. During these intensive observational periods (IOPs), we performed additional

Table 2. Overview and availability of the continuously running ground-based instrumentation during the CROSSINN field campaign. The remote sensing instruments are grouped according to the parameters they measure. The device name specifies how the instruments are referred to in the manuscript and allows us to distinguish between the different Doppler lidars. Due to a faulty automatic calibration, profiles from the HATPRO-G4 are only available after 17 August, while the integrated variables are usable from the beginning of the campaign. Abbreviations: University of Innsbruck (UIBK) and Karlsruhe Institute of Technology (KIT). The instruments operated by KIT are part of the mobile observation platform KITcube (Kalthoff et al. 2013), the surface flux towers are part of the i-Box (Rotach et al. 2017), and the UIBK Doppler lidars are part of the i-Box and the Innsbruck Atmospheric Observatory (Karl et al. 2020).

Parameter	Device name	Type	Manufacturer	Operator	Site name	Operation period
Meteorological parameters, radiation, turbulence	i-Box	Surface flux towers (1–3 levels)	Various	UIBK	Kolsass, Terfens, Eggen, Weerberg, Hochhäuser, Arbeser	1 Aug–13 Oct
Wind	Windcube 200s	Doppler lidar	Leosphere	KIT	Mairbach, Kolsass, Hochhäuser	1 Aug–13 Oct
	Streamline	Doppler lidar	Halo Photonics	UIBK	Kolsass	1 Aug–10 Oct
	Streamline XR	Doppler lidar	Halo Photonics	UIBK	Kolsass	1 Aug–10 Oct
	Wind Ranger	Doppler lidar	METEK GmbH	METEK GmbH	Kolsass	1 Aug–9 Sep
Temperature, humidity	HATPRO-G4	Microwave radiometer	Radiometer Physics	KIT	Kolsass	(1 Aug) 17 Aug–13 Oct
	HATPRO-G3	Microwave radiometer	Radiometer Physics	UIBK	Innsbruck	1 Aug–13 Oct
	Temperature lidar	Raman lidar	Raymetrics S.A.	Raymetrics S.A.	Kolsass	1 Aug–8 Aug, 25 Aug–2 Oct
Clouds, backscatter	CHM 15k	Ceilometer	Lufft GmbH	KIT	Kolsass	1 Aug–13 Oct
Clouds	MX-S15D	Visible and infrared camera	Mobotix AG	KIT	Kolsass	1 Aug–13 Oct

radiosonde (manufactured by GRAW) and aircraft measurements to obtain highly resolved information on the vertical structure of the MoBL and its spatial variability in the Inn Valley.

Within the 2.5 months of the field campaign, we performed 10 IOPs in total, 7 of them in August and 3 in September (Fig. 3). An IOP usually started at 0500 local time (LT = UTC + 2 h) and lasted for 24 h to capture the whole diurnal cycle of the thermally driven circulations and the MoBL. During an IOP, we launched 10 radiosondes at 2–4-hourly intervals. As we expected changes in the MoBL structure to be strongest in the afternoon, the

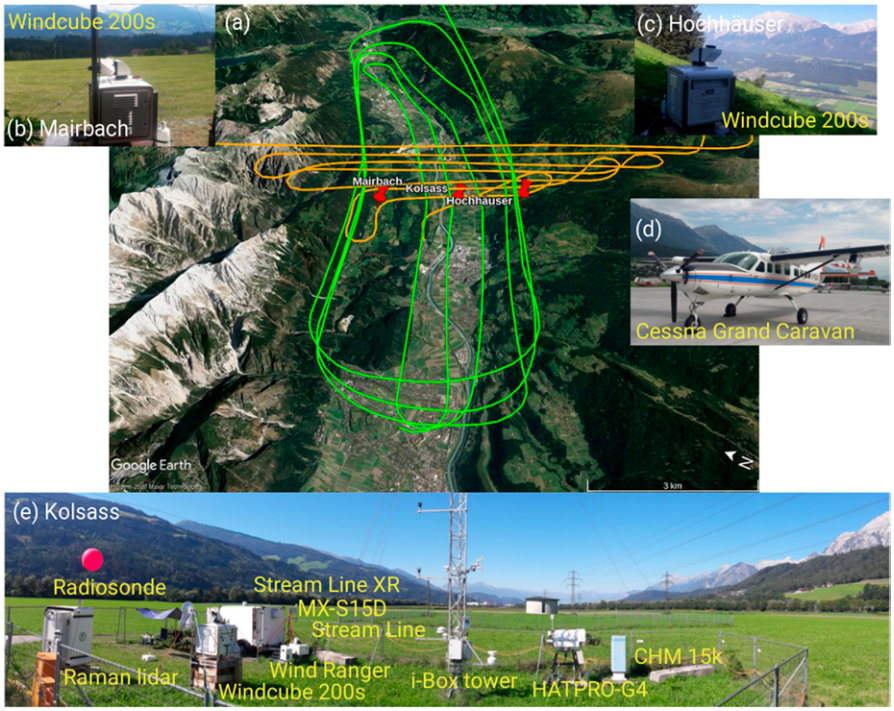

Fig. 2. (a) Investigation area in the Inn Valley (map data: Google Earth 2020, Maxar Technologies) with the cross- and along-valley flight legs of (d) the DLR Cessna Grand Caravan 208b indicated in orange and green, respectively. Photographs of CROSSINN instrumentation at the three ground-based sites at (b) Mairbach, (c) Hochhäuser, and (e) Kolsass. For device names, see Table 2.

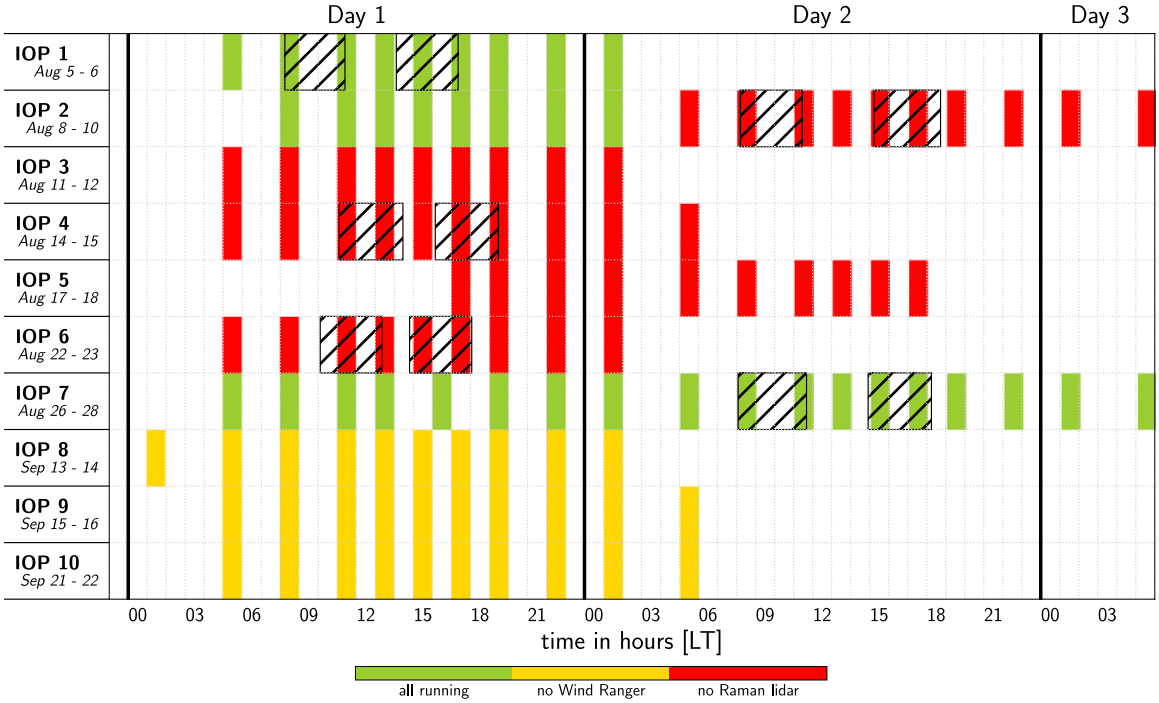

Fig. 3. Overview of the CROSSINN IOPs during August and September 2019. The first and the last radio soundings indicate the start and end of each IOP. Radiosonde ascent periods are given by the colored bars starting at the launch time. Aircraft flight periods are given by the hatched areas. The individual colors indicate the availability of ground-based instrumentation: every device was running (green), every device was running except for the Wind Ranger (yellow), and every device was running except for the temperature lidar (red). The Wind Ranger was not available during the last three IOPs, as it had to be taken down on 9 Sep and the temperature lidar did not work during most of the IOPs in August due to air conditioning defects.

intervals of the radiosonde launches were shortest between 1100 and 1900 LT. Due to the vicinity of Innsbruck Airport, every radiosonde launch had to be coordinated with the tower there by phone. Unfavorable weather conditions during IOPs 5 and 8 (i.e., rain, clouds, or strong synoptically driven changes) forced a change of the measurement periods, while favorable weather conditions during IOPs 2 and 7 allowed for extending the IOPs to 48 h.

Wind measurements. In total, six Doppler lidars were operated during the campaign (Table 2), four at Kolsass and one each at Mairbach and Hochhäuser (locations in Fig. 1c). The chosen scan settings (Table 3) were compromises between obtaining good maximum measurement ranges and still resolving the flow structures on a scale of a few hundred meters.

The backbone of the campaign were three scanning Windcube 200s lidars manufactured by Leosphere (Tables 2 and 3). All three lidar sites were aligned along a line roughly perpendicular to the valley axis (Fig. 1c) at Mairbach (854 m MSL, on the plateau in the northern part of the valley), Kolsass (546 m MSL, in the valley center), and Hochhäuser (1,081 m MSL, on the southern slope), respectively. The lidar sites were a trade-off between technical requirements, i.e., the distance between the lidars had to be small enough to have overlapping measurements and large enough to have the beams intersect at sufficiently large angles, and logistical constraints, such as permission of landowners, power supply, and a free line of sight over the valley. This resulted in a small offset of the planes spanned by the lidars in along-valley direction of 120 m at the maximum. The three lidars performed synchronized continuous coplanar RHI scans at an azimuth angle of 158.15° to measure the radial velocity across the valley. The lidar at Kolsass scanned the whole upper half space, while the scan sectors of the lidars at Mairbach and Hochhäuser were smaller due to topographic limitations (Fig. 4a, Table 3). The steep slope at Hochhäuser allowed us to start at the smallest possible elevation angle of –19° below the horizon. Each RHI scan lasted 60 s. The lidars were controlled using an API (Application Programming Interface) provided by Leosphere, which interrupted the measurements twice a day for a wipe and lubrication to prevent damage to the scanner head. The RHI scans were started simultaneously with each lidar at the full minute and were done continuously from south to north and back from north to south.

Table 3. Technical specifications and scan settings of the Doppler lidars. For the pulsed Windcube and Streamline lidars, temporal resolution describes the accumulation time, while for the continuous-wave Wind Ranger lidar it describes the time increment at which measurements are available at the respective height. Physical resolution reflects the length of the volume (range gate) for which the radial velocity is determined and range gate distance describes the distance between the range gate centers. Measurement ranges are given at the center of the range gates. The Streamline XR performed a combination of vertical stare and PPI at different elevation angles. Abbreviations: range–height indicator (RHI), plan position indicator (PPI), and velocity azimuth display (VAD).

Device	Windcube 200s	Windcube 200s	Windcube 200s	Streamline XR	Streamline	Wind Ranger
Site	Mairbach	Kolsass	Hochhäuser	Kolsass	Kolsass	Kolsass
Scan mode	RHI	RHI	RHI	Vertical/PPI	PPI	VAD
Wavelength (μm)	1.54	1.54	1.54	1.5/1.5	1.5	1.55
Temporal resolution (s)	0.25	0.25	0.25	1/1	1	~13
Physical resolution (m)	100	100	100	57/57	26.25	0.1, 0.4, 4.1, 12.0, 16.0
Range gate distance (m)	50	50	50	36/36	36	Variable
Measurement range (m)	200 to 6,150	200 to 6,150	200 to 6,150	108 to 7,164	54 to 2,970	7.9, 16.1, 50.5, 84.8, 100
Angular resolution (°)	0.51	0.76	0.60	—/3	6	—
Scan speed (° s^{-1})	2.04	3.04	2.40	—/3	6	360
Elevation angle (°)	–10 to 112.4	0 to 182.4	55 to 199	90/4, 7, 70	70	80
Azimuth angle (°)	158.15	158.15	158.15	—/0 to 359	0 to 359	0 to 359

Every 60 s, a set of three RHI scans was obtained, which was then used for the retrieval of the cross-valley two-dimensional wind field consisting of a horizontal and vertical component in the vertical plane (Fig. 4). For the retrieval of the two-dimensional wind field, overlapping coplanar scans from two Doppler lidars are sufficient and this setup has been used successfully to study, for example, nocturnal flow phenomena in a meteor crater basin in Arizona (Whiteman et al. 2018), wakes induced by a wind turbine between two parallel mountain ridges (Wildmann et al. 2018), and coherent structures in the surface layer over flat terrain (Newsom et al. 2008; Träumner et al. 2015). During CROSSINN, we combined coplanar RHI scans from three Doppler lidars, as this considerably enlarges the area in which the wind field can be retrieved (Fig. 4f). The algorithm used to calculate the two-dimensional wind field in the vertical plane is described in detail by Haid et al. (2020) and was also applied by Adler et al. (2020) to coplanar horizontal Doppler lidar scans. The corresponding Python code is available on GitHub (Haid 2019). In a first step, the radial velocity fields from all three lidars were filtered for outliers by applying a threshold filter to the carrier-to-noise ratio (–28 dB), a hard target filter to eliminate data influenced by the surface or clouds, a jump filter of 2 m s^{-1} to identify rapid, unrealistic changes in radial velocity at each range gate for successive time steps (0.25 s increments), and a median absolute deviation filter. The radial velocity measurements from the RHI scans are not exactly collocated. Because of this, the two-dimensional wind vector is retrieved on a Cartesian grid with a lattice length of Δl = 50 m spanning the vertical scanning plane (Fig. 4a). To each grid point of the Cartesian grid, radial velocity measurement values from all three lidars are assigned within a certain radius $R = \Delta l/\sqrt{2}$ of the grid point and the intersection angle of the individual lidar beams is calculated. To prevent too large propagation errors arising when the individual lidar beams are nearly colinear, we considered only grid points for which the intersection angle was between 30° and 150° for at least two of the lidars, following the suggestion by Träumner et al. (2015). The most probable horizontal wind component along the vertical plane and vertical wind component were deduced for every grid point by minimizing a cost function (e.g., Newsom et al. 2008; Stawiarski et al. 2013). The limitations due to the actual measurement ranges of the lidars depending on backscatter and intersection angles constrain the grid points where the wind vector can be retrieved. For example, the retrieval was not possible close to the slopes (Figs. 4e,f). On days with good measurement ranges, i.e., when enough backscatter was present, it was possible to retrieve the wind field in a vertical plane of about 6 km horizontal and 3 km vertical extent (Fig. 4e). The radial velocity fields measured by the individual lidars (Figs. 4b–d) revealed several vertical layers in which the radial velocity changed sign. By combining them to retrieve the two-dimensional wind field, a deep layer is visible between about 1,000 and 2,500 m above the valley floor (AVF) with a strong (>10 m s^{-1}) southerly wind component and waves in the shear zone at the bottom (Fig. 4e). The varying number of lidars available for the retrieval of the wind vector at the individual grid points apparently does not impair the consistency of the retrieved wind field (Figs. 4e,f).

The Halo Photonics Streamline and Streamline XR Doppler lidars were installed at the Kolsass measurement site (Tables 2 and 3 and Figs. 1c and 2e). The Streamline lidar was mounted at ground level and the Streamline XR lidar at approximately 2 m above ground level in a trailer. The Streamline lidar performed 360° plan-position-indicator (PPI) scans at an elevation angle of 70° continuously throughout the campaign with a repetition rate of around 80 s. To extend the maximum vertical range of the horizontal wind profiles, the more powerful Streamline XR lidar additionally performed PPI scans at a 70° elevation angle every half hour. Assuming horizontal homogeneity, vertical profiles of the three-dimensional wind vector were estimated from the PPI scans at a 70° elevation angle by applying the velocity azimuth display (VAD) method (Browning and Wexler 1968) and by solving an overdetermined system of linear equations for each height using the weighted least squares approach. The assumption

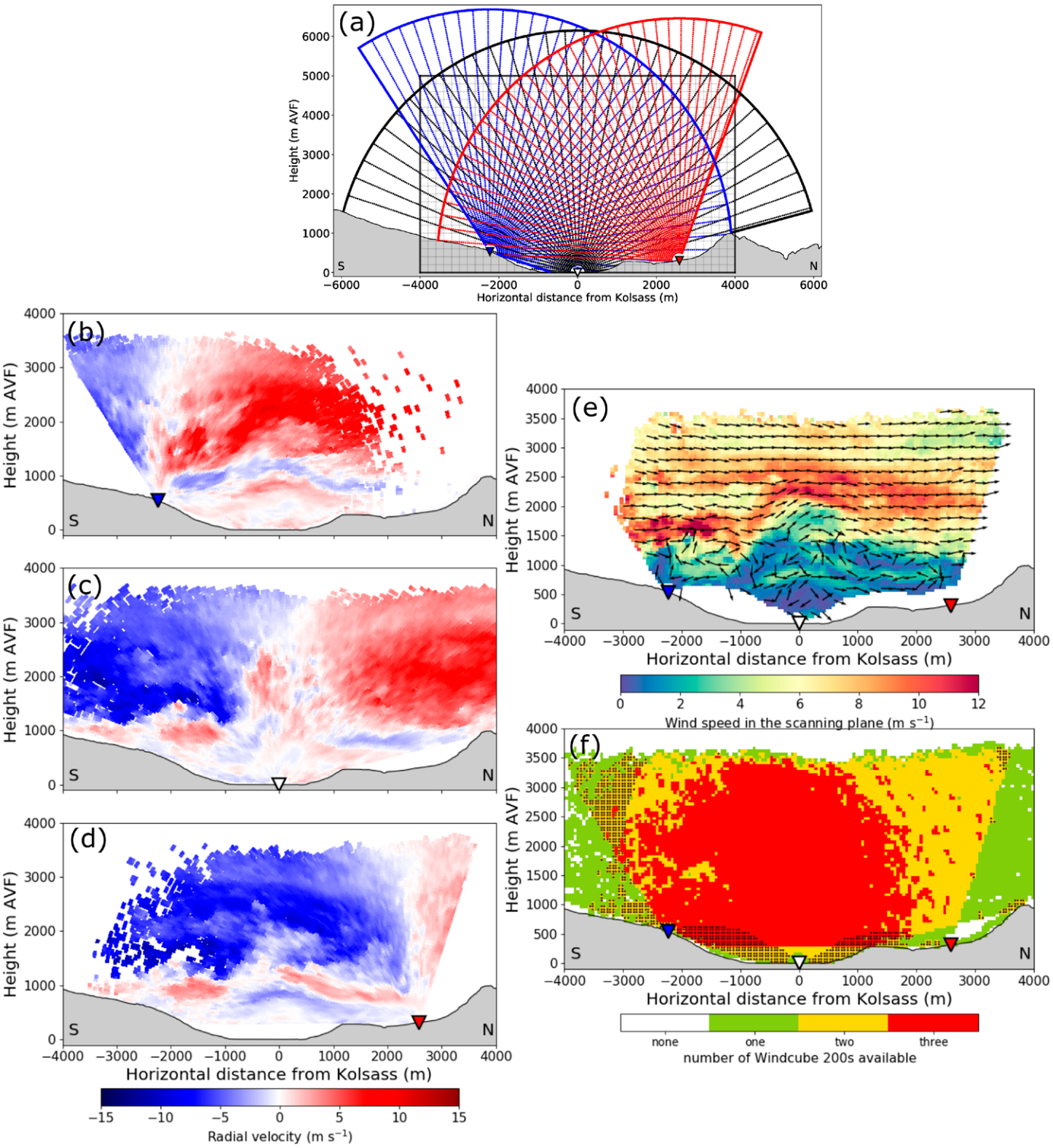

Fig. 4. (a) Schematic representation of the coplanar RHI scans of the three Windcube 200s lidars at Hochäuser (blue), Kolsass (black), and Mairbach (red). The rectangular gridded area indicates the area where the two-dimensional cross-valley wind is retrieved in the vertical plane. For better visibility, only every sixth ray of the RHI scans and every fourth grid line of the Cartesian grid are shown. Radial velocity measured by the Windcube 200s lidars at (b) Hochäuser, (c) Kolsass, and (d) Mairbach during a simultaneous RHI scan at 1725 LT during IOP 3. (e) Retrieved two-dimensional cross-valley wind vectors (horizontal and vertical components) in the scanning plane (arrows) and wind speed (color-coded) and (f) number of lidars available at the individual grid points to calculate the two-dimensional wind vectors (color-coded). Dots in (f) mark the grid points that are excluded by the intersection angle criteria.

of horizontal homogeneity does not always hold over mountainous terrain, which may induce errors in the horizontal wind speed on the order of 10% (Bingöl et al. 2009). Besides the two PPI scans at an elevation angle of 70°, two different scan patterns were performed with the Streamline XR lidar: during the first 30 min period of each hour, the Streamline XR measured in vertical stare mode, which directly provides the vertical velocity at 1 Hz frequency. In the second half-hourly period, the lidar performed 360° PPI scans at elevation angles of 4° and 7°. The PPI scans were executed one after the other. In total, 12 scans, 6 at each elevation angle, were conducted within the 30 min period.

Unlike the pulsed Windcube and Streamline lidars, the Wind Ranger is a continuous-wave lidar developed by METEK GmbH (Peters 2018) for a small minimum measurement range and fine range resolution (Tables 2 and 3 and Fig. 2e). The range-dependent radial velocity is obtained by changing the focal point of the lidar beam and by a frequency modulation of the returned signal with a triangular pattern. From the radial velocity measurements, the three wind components were retrieved using the VAD method. The Wind Ranger was set to measure sequentially at five heights (Table 3). A whole cycle lasted around 13 s with a measurement duration of roughly 1 s per height. This means that at each height, time series of the three-dimensional wind were available with a temporal resolution of about 13 s.

Temperature and humidity measurements. The Raymetrics temperature lidar installed at Kolsass (Table 2 and Fig. 2e) is based on the rotational Raman (RR) technique, where the relative intensity of two spectral regions of the molecular rotational Raman spectrum is used to estimate ambient temperature. The lidar is based on a monoaxial design, i.e., the laser beam propagation axis and the receiving telescope optical axis coincide. It is equipped with a Single Longitudinal Mode Nd:YAG laser (manufactured by Quantel/Lumibird), emitting 200 mJ per pulse at 355 nm at 10 Hz repetition rate and 6–8 ns pulse duration. The specific prototype used during CROSSINN was not eye-safe. The receiving telescope is a 400 mm Classical Cassegrain. The field of view can be adjusted from 0.25 mrad up to 1 mrad depending on the field stop diameter. For the measurements performed within the CROSSINN field campaign, it was set to 0.6 mrad. The telescope is shielded by a fused silica window with an appropriate antireflection coating. The system is equipped with five detection channels. These are the elastic channel at 354.78 nm for retrieving the aerosol backscatter coefficient, two rovibrational Raman channels at 387 and 407 nm for retrieving aerosol extinction and water vapor mixing ratio, and two RR channels approximately at 355.5 and 356 nm to retrieve atmospheric temperature profiles (Reichardt et al. 2012). Hamamatsu photomultipilier tubes detect simultaneously in both analog and photon-counting modes. The system provides temperature profiles for altitudes ranging from 500 m (full lidar system overlap) up to 3,500 m during day time. The raw spatial and temporal resolutions of the lidar files are 7.5 m and <1 min, respectively. The final spatial and temporal resolutions after processing are user-adjustable and range from 60 to 900 m and from 10 to 90 min (standard 30 min), respectively. The processing of the temperature lidar data are currently ongoing.

A scanning microwave radiometer HATPRO-G4 at Kolsass (Table 2 and Fig. 2e) measured atmospheric emission at 14 frequencies, from which temperature and humidity profiles, integrated water vapor (IWV) and liquid water path (LWP) were obtained with a retrieval algorithm provided by the University of Cologne (Crewell and Löhnert 2003; Löhnert et al. 2009). The complex terrain of the Inn Valley and the fact that mainly nighttime radiosonde profiles measured at Innsbruck airport between 2013 and 2019 were available for the retrieval training may challenge the retrieval performance as discussed in Massaro et al. (2015). The accuracy of the temperature profiles in low levels is enhanced by measuring at low elevation angles along the valley axis every 10 min (Crewell and Löhnert 2007). Every 30 min, a PPI scan at

an elevation angle of 20.65°, i.e., just above the ridges north and south of the site, was done to retrieve spatial information on the IWV and LWP distribution. Adler and Kalthoff (2014) showed that these kinds of scans are suitable to detect the water vapor transport with slope winds. A second microwave radiometer HATPRO-G3 is permanently installed at Innsbruck on the roof top of the university building (Table 2).

Cloud and backscatter measurements. Information on cloud base heights and coverage was obtained with a ceilometer CHM 15k and a camera system (Table 2 and Fig. 2e). Recordings of the sky were taken every 60 s with a fish-eye image in the visible spectral range and with an aperture angle of 45° in the thermal (7.5–13.5 μm) and visible ranges. From the CHM 15k measurements, up to three cloud base heights were calculated automatically every minute with the manufacturer algorithm using a threshold method. In addition, the CHM 15k measured uncalibrated backscatter profiles up to 15,000 m with a vertical resolution of 15 m averaged over 60 s.

i-Box towers. The six i-Box surface flux towers in the investigation area measure turbulence at up to three levels with sonic anemometers and fast-response hygrometers, radiation, soil moisture, and soil heat flux, as well as standard meteorological parameters, such as temperature, humidity, wind, pressure, and precipitation (Table 2 and Figs. 1b,c). The equipment at the different sites varies, with Kolsass being the site best equipped with instruments measuring the radiation balance, precipitation and turbulence, and wind at 4, 8.7, and 16.9 m above the ground. A detailed overview of the instrumentation and measurement heights at the different sites is given in Rotach et al. (2017).

Airborne measurements. Aircraft flights were performed with the Cessna Grand Caravan 208 B of the German Aerospace Center (DLR) (Fig. 2d) on five IOPs (IOPs 1, 2b, 4, 6, and 7b; Fig. 3) which fell into the period from 5 to 27 August, during which the aircraft was available. The aim was to measure the spatial variability of meteorological parameters in a vertical north–south–oriented cross section above Kolsass and in an along-valley west–east pattern along the Inn Valley (Fig. 2a). In situ measurements of temperature, humidity, and wind with 100 Hz temporal resolution were obtained with a meteorological sensor package (METPOD) mounted underneath the left wing of the aircraft. A detailed description of the instruments and measurement accuracy is given in Mallaun et al. (2015).

The planning of the aircraft flights was strongly facilitated by previous aircraft flights performed in the same section of the Inn Valley in 2013 (Baur 2015). During each of the five IOPs, the first flight was conducted in the morning during the expected last stage of the downvalley wind, while the second flight took place in the afternoon when the upvalley wind was likely established (Fig. 3). As the Inn Valley was filled with low-level clouds in the morning of IOPs 4 and 6, the morning flights on these days had to start later (Fig. 3). Roughly 3 h of each flight were spent in the Inn Valley, the remaining flight time was required for the ferry from and to the airport at Oberpfaffenhofen in the Alpine foreland near Munich (Fig. 1a) and for landing and takeoff at Innsbruck airport for refueling between the morning and afternoon flights.

The flight scenarios consisted of two main patterns (Fig. 2a). The first pattern comprised eight stacked legs in cross-valley direction with the upper seven legs in the same plane as the coplanar Doppler lidar measurements. The lowest leg had to be turned slightly in along-valley direction because of the terrain. The legs were flown with a vertical offset of around 300 m, with the lowest leg at around 400 m AVF and the highest leg at around 3,000 m, i.e., a few hundred meters above the surrounding mountain ridges. The second pattern consisted of four elongated boxes in along-valley direction of more than 10 km length with two roughly

straight legs flown close to the southern and northern slopes, respectively. The along-valley legs in the upper three boxes were approximately 5.5 km apart, while the legs in the lowest box at around 400 m AVF were about 2 km apart. One leg was flown along the valley center at around 250 m AVF. Both patterns were flown twice during each flight, starting with the cross-valley pattern.

Initial analysis

Campaign overview. Figure 5 and Table 4 give an overview of the atmospheric conditions during the whole measurement campaign and the IOPs. The synoptic situation was a mix between periods with frequent trough passages associated with relatively strong large-scale westerly wind, clouds, and precipitation and more quiescent, dry periods with a weaker large-scale pressure gradient and fewer clouds. The method proposed by Lehner et al. (2019) was applied to identify synoptically undisturbed, clear-sky days based on a clear-sky index and geopotential height fields from ERA5. ERA-Interim, for which the method was originally

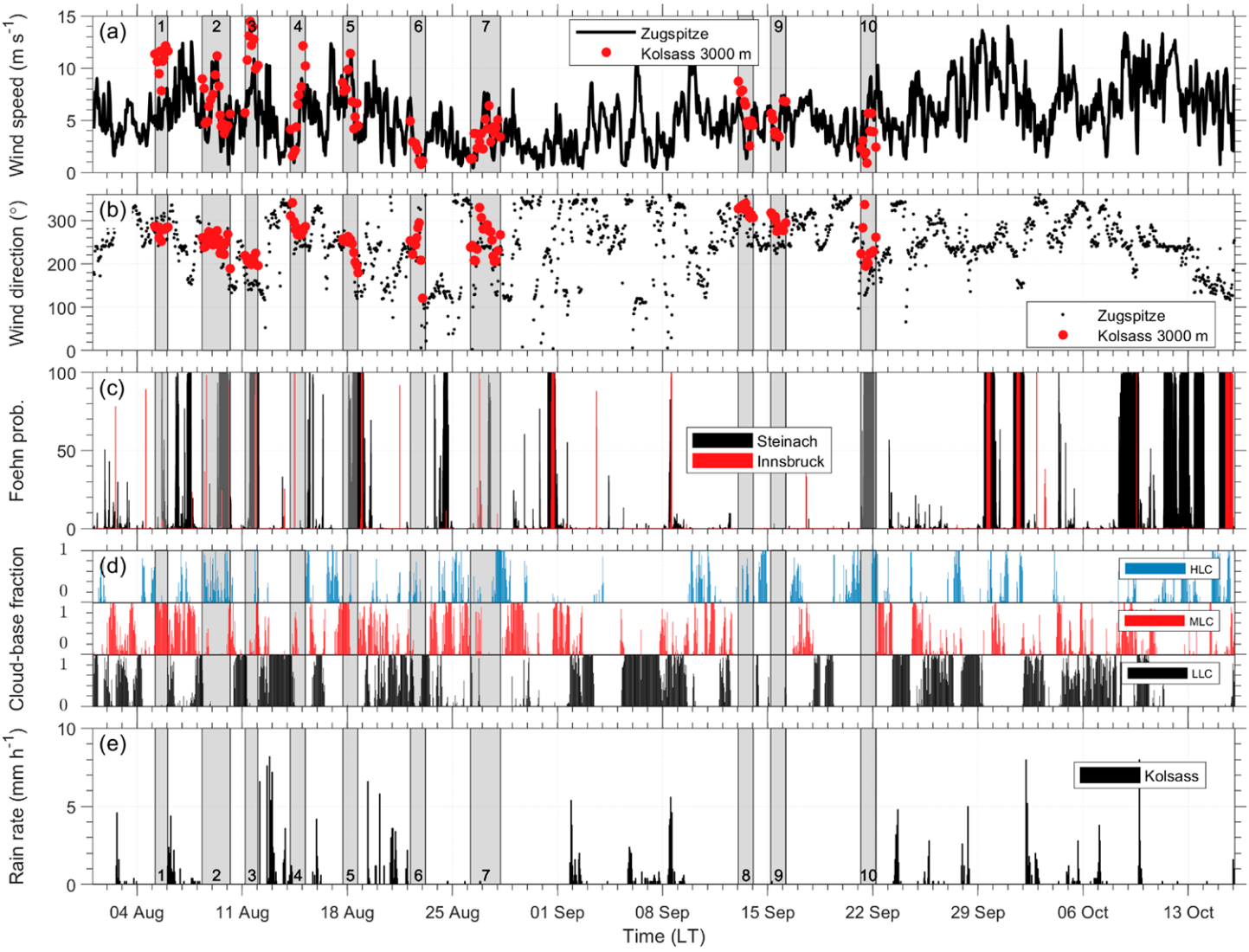

Fig. 5. Overview of atmospheric conditions during the CROSSINN field campaign in 2019. (a),(b) Horizontal wind speed and direction measured at the top of Mt. Zugspitze at around 3,000 m MSL and at 3,000 m MSL from radio soundings at Kolsass. (c) Foehn probability at Steinach in the Wipp Valley and Innsbruck based on the foehn diagnosis from Plavcan et al. (2014). (d) The 1 h cloud-base fraction of low-level (LLC; 0–3,000 m MSL), midlevel (MLC; 3,000–6,000 m MSL), and high-level (HLC; >6,000 m MSL) clouds measured by the CHM 15k at Kolsass. (e) Rain rate measured at the i-Box tower at Kolsass. The gray vertical columns indicate the IOP periods.

Table 4. Synopsis of atmospheric conditions during IOPs. Mean wind direction and speed at 3,000 m MSL are averages from all radiosonde profiles at Kolsass during the respective IOP. The foehn probability for Steinach in the Wipp Valley is based on the foehn diagnosis of Plavcan et al. (2014). The upvalley wind characteristics are retrieved from the horizontal wind profiles measured with the Streamline Doppler lidar at Kolsass. The integrated heat deficit is calculated from the potential temperature (Θ) radiosonde profile at 1700 LT at Kolsass for the layer from the valley floor up to the mean ridge height at 1,630 m MSL.

IOP	Date	Mean wind direction (°) and speed (m s^{-1}) at 3,000 m MSL	Duration of 100% foehn probability at Steinach (h)	Value (m s^{-1})/height (m AVF)/time (LT) of maximum upvalley wind	Integrated heat deficit $\frac{1}{h_{\text{ridge}}-h_{\text{VF}}}\int_{h_{\text{VF}}}^{h_{\text{ridge}}}\left[\Theta_{\text{ridge}}-\Theta(z)\right]dz$ (K)
1	5–6 Aug	276/10.2	0.0	3.8/ 186/1450	2.4
2a	8–9 Aug	257/6.6	0.0	12.1/220/2000	0.7
2b	9–10 Aug	247/5.6	4.2	7.1/321/1940	1.0
3	11–12 Aug	208/11.7	10.0	6.9/254/1840	2.9
4	14–15 Aug	281/5.0	0.0	9.8/254/1820	0.8
5	17–18 Aug	236/6.3	8.0	8.7/321/1830	0.8
6	22–23 Aug	248/2.4	0.0	13.3/355/2100	4.0
7a	26–27 Aug	261/2.2	0.0	6.0/491/1500	0.9
7b	27–28 Aug	256/3.7	0.0	9.9/457/1950	1.1
8	13–14 Sep	328/5.5	0.0	12.9/254/1800	2.6
9	15–16 Sep	296/4.0	0.0	8.8/693/2040	2.4
10	21–22 Sep	231/2.4	14.7	8.1/288/1720	2.6

developed, was no longer available after 31 August 2019. As ERA5 has a higher horizontal resolution, the ERA5 fields are smoothed three times by a box average of 5 × 5 grid points and horizontal gradients are calculated over six grid points instead of two. By applying this modification, 87% of the days previously identified with ERA-Interim can be reproduced. The method is extremely strict and selects only completely undisturbed days, which are most perfect for thermally driven circulations. Only one day during the CROSSINN field campaign period fulfilled the stringent criteria, which is on the low end compared to previous years (0–11 valley-wind days for the same period during the years 2014–18). Note that valley winds form far more frequent in the Inn Valley and may develop even under the influence of synoptic forcing, i.e., large-scale wind (Zängl 2009). According to Vergeiner and Dreiseitl (1987), 29% of all days exhibit valley-wind characteristics such as the twice-daily wind reversal. However, they only found one completely undisturbed day in their 4-yr-long dataset.

Wind speed and direction measured at Mt. Zugspitze, a nearly 3,000-m-high peak northwest of the investigation area (Fig. 1a), and at 3,000 m MSL with the radio soundings at Kolsass during the IOPs were used as a proxy for the large-scale flow (Figs. 5a,b). During the first three weeks of the campaign, the investigation area was often affected by trough passages reflected by a relatively strong wind speed, with only brief periods of shortwave ridging, during which IOPs 1–5 were conducted. After around 22 August, the large-scale pressure gradient weakened, leading to mean large-scale wind speed values during IOPs 6 and 7 of 2–4 m s^{-1} only (Table 4). From 2 September, troughs became the dominant pattern again, before another rather quiescent period with a relatively weak large-scale pressure gradient developed between 12 and 23 September, during which IOPs 8–10 were conducted. After that, unsettled weather and strong winds continued through the end of the campaign in mid-October.

In case of a moderate to strong southerly large-scale flow component, the Inn Valley may be affected by south foehn which strongly influences the MoBL conditions and interacts with the thermally driven circulations. To assess the likelihood of foehn in the investigation

area, we used the foehn probability at Steinach in the Wipp Valley and Innsbruck in the Inn Valley (Fig. 1a) which is based on the method of Plavcan et al. (2014) (Fig. 5c and Table 4). The method diagnoses foehn automatically and probabilistically using a statistical mixture model. The variables considered are wind direction and speed at the stations in the valleys and the potential temperature difference between the valley stations and a station higher up. For Innsbruck relative humidity is additionally taken into account. During four IOPs (IOPs 2b, 3, 5, and 10), foehn likely prevailed for several hours judging from the probability at Steinach. Foehn at Innsbruck in the Inn Valley occurs less often than at Steinach in the Wipp Valley. This indicates that foehn more frequently breaks through to the valley floor at Steinach than at Innsbruck. The latter is about 500 m lower than the station elevation at Steinach and often affected by a cold air pool (e.g., Haid et al. 2020).

Given the large number of days with clouds during the campaign, we were quite successful in choosing days with no or few clouds in the Inn Valley for the IOPs (Fig. 5d). During IOPs 2a, 3, 4, 6, and 7a, low-level clouds filled the Inn Valley at sunrise, but disappeared during the morning. Some mid- and high-level clouds occurred during IOPs 1, 2, 5, and 8. Although no major precipitation events occurred within the IOPs (Fig. 5e), IOP 2 had to start later and IOPs 1 and 3 had to finish earlier (Fig. 3) due to precipitation. Some convective showers affected the Inn Valley in the afternoon of IOPs 1 and 7a.

This high variability of large-scale conditions resulted in quite substantial differences in the timing and strength of the upvalley wind and in the stratification in the Inn Valley during the IOPs (Table 4). The maximum upvalley wind speed varied between 3.8 m s^{-1} (IOP 1) and 13.3 m s^{-1} (IOP 6) and the height of the maximum ranged from 220 m AVF (IOP 2a) to 693 m AVF (IOP 9). The maximum value occurred as early as 1450 LT (IOP 1) and as late as 2100 LT (IOP 6). The weak upvalley wind and the early occurrence of its maximum during IOPs 1 and 7a are likely related to the occurrence of moist convection in the afternoon which disturbed the further persistence and intensification of the upvalley wind. The integrated heat deficit (defined in Table 4) is used as a proxy for stratification, i.e., the smaller the value, the closer the valley atmosphere to being well mixed. While the stratification in the valley was quite close to neutral in the afternoon during some IOPs (e.g., IOPs 2a, 4, 5), large deficits remained during others (e.g., IOPs 3, 6). To illustrate how the set of observations can be used to study the three-dimensional flow structure and thermodynamic conditions in the MoBL, mainly data from IOP 8 are presented below as an example.

Evolution of the vertical MoBL structure in the valley center. The profiling instruments at Kolsass provide essential information about the temporal evolution of temperature, humidity and wind profiles and, hence, about the evolution of the MoBL in the valley center. To obtain information on these variables in the valley and above the ridges, radiosonde profiles are still invaluable, as they cover the whole troposphere and measure regardless of backscatter, rain, or clouds. During IOP 8, northwesterly wind prevailed above the ridge height and decreased in strength in the course of the IOP (Figs. 5a,b and 6a). From the beginning of the IOP at 0100 LT to sunrise at around 0730 LT, the atmosphere in the valley was stably stratified with a potential temperature increase of around 15 K from the surface to the mean ridge height (Fig. 6a). The stability was rather constant with height in this layer and did not change much with time. Only the lowest layer adjacent to the surface cooled continuously over the night by around 3 K. After around 0200 LT, the downvalley wind established and filled the larger part of the valley (Figs. 6a,b). It gradually increased in strength and reached its maximum of around 5 m s^{-1} at 0900 LT.

After local sunrise at Kolsass at around 0730 LT, surface-based convection started as visible from the i-Box tower measurements (not shown) and a shallow neutrally stratified layer—identified in the radiosonde profiles by visual inspection—developed slowly and reached up

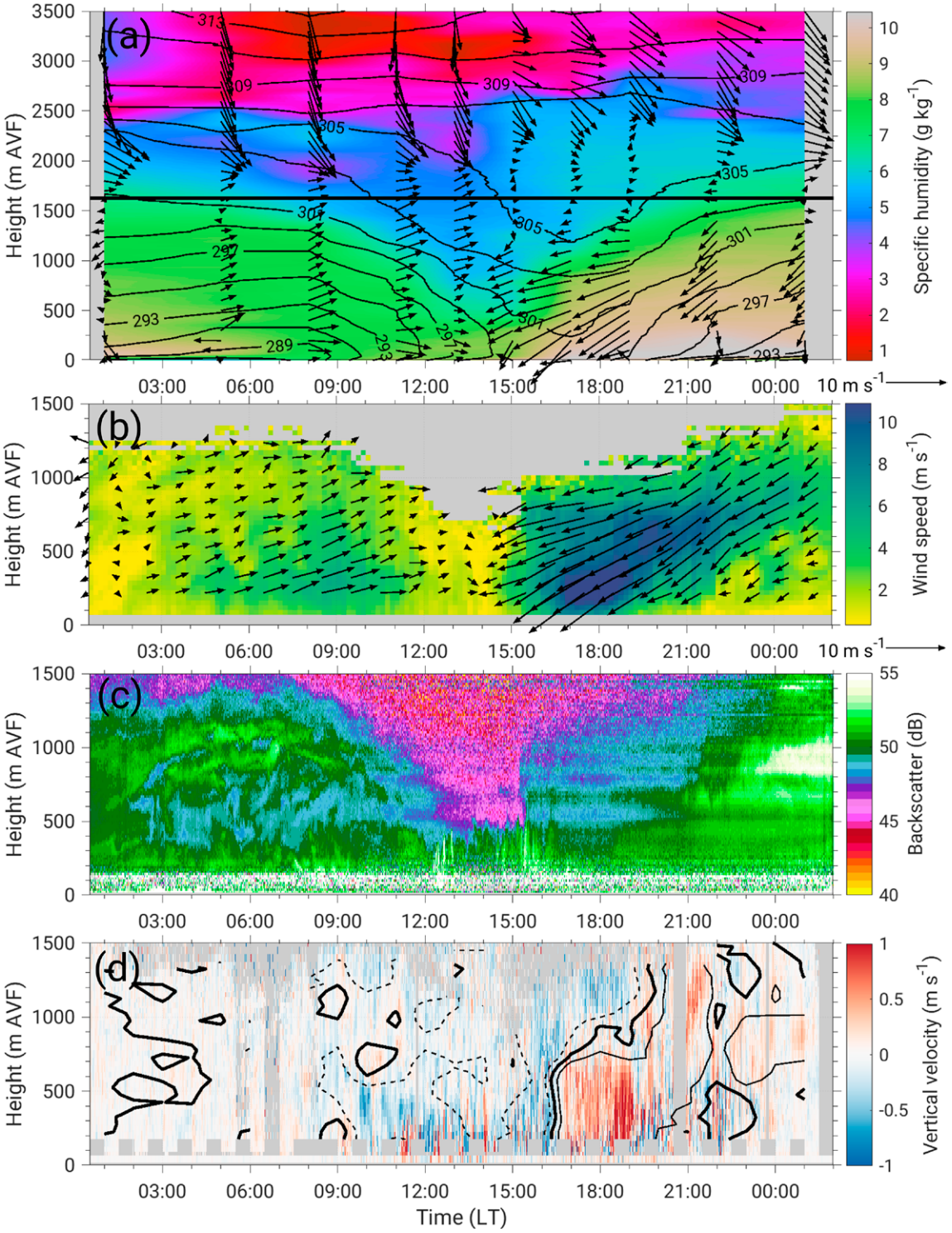

Fig. 6. Time–height sections at Kolsass during IOP 8 (13–14 Sep): (a) specific humidity (color-coded), potential temperature (black isolines, K) and horizontal wind vector (arrows) measured by radiosondes. The horizontal black line indicates the mean ridge height. (b) Horizontal wind speed (color-coded) and horizontal wind vector (arrows) measured by the Streamline Doppler lidar. (c) Backscatter measured by the CHM 15k (color-coded). (d) Vertical velocity (color-coded, red indicates upward motion and blue downward motion) measured by the Streamline XR and Windcube 200s lidars and 1 h averaged vertical velocity [black isolines indicate –0.1 (dashed), 0 (thick solid), and 0.1 m s^{-1} (thin solid)] measured by the Windcube 200s. The lowest row (16.9–66.9 m AVF) shows the 1 min averaged vertical velocity measured at 16.9 m AVF at the i-Box tower. Specific humidity and potential temperature profiles are temporally linearly interpolated between the radiosonde launch times.

to around 300 m AVF at 1300 LT (Fig. 6a). Over horizontally homogeneous and flat terrain, this layer would be interpreted as the mixed layer portion of the convective boundary layer. Within this neutrally stratified layer, convective updrafts were visible in the Doppler lidar measurements after around 1100 LT (Fig. 6d). As the lowest usable range gate of the Streamline XR in the vertical stare mode and of the Windcube 200s when passing zenith was at 108 m AVF and 200 m AVF, respectively, convective cells had to reach a certain height to be detected by the lidars. During IOP 8, this was the case after around 1100 LT only. In general, this measurement gap could be closed by the Wind Ranger lidar—unfortunately, it was not available for the presented IOP (Fig. 3).

In the course of the morning, the whole valley atmosphere warmed by several degrees, stability decreased, and a weakly stably stratified layer formed between around 1,200 and 2,500 m AVF (Fig. 6a). The vertical layering resembles the typical three-layer structure often found in valleys, where the shallow neutrally stratified layer (below 300 m) corresponds to the lower mixed layer and the weakly stably stratified layer (between 1,200 and 2,500 m) to the upper mixed layer. The layer in between may be interpreted as the stable valley atmosphere. Potentially warm, dry air (Fig. 6a) with a low backscatter (Fig. 6c) subsided into the valley. Mean subsidence on the order of centimeters per second was measured by the Windcube 200s at Kolsass (Fig. 6d). The top of the layer with the higher backscatter detected by the CHM 15k between 1100 and 1500 LT agrees well with the neutrally stratified layer visible in the radiosonde profile (Figs. 6a,c). The low backscatter strongly reduced the vertical range of the Doppler lidar wind profiles (Figs. 6b,d), which is one of the major drawbacks of Doppler lidars.

After a transition phase with a weak horizontal wind speed of less than 2 m s^{-1}, the upvalley wind established after around 1400 LT and abruptly increased in strength to more than 4 m s^{-1} at around 1530 LT (Figs. 6a,b). This rapid strengthening was associated with an increase in specific humidity (Fig. 6a) and backscatter (Fig. 6c) which likely indicated the arrival of a different air mass advected by the upvalley wind. After the onset of the upvalley wind, the top of the neutrally stratified layer decreased to around 200 m AVF at 1700 LT (Fig. 6a) and mean subsidence of up to 0.3 m s^{-1} dominated throughout the measurement range up to around 1,000 m AVF with some embedded convective cells (Fig. 6d). Shortly before 1700 LT, the upvalley wind speed rapidly increased further to values of more than 11 m s^{-1} at the height of its maximum near 250 m AVF and stayed strong until around 1900 LT (Figs. 6a,b). This was associated with continuous upward motion of nearly 0.6 m s^{-1} on the average below around 700 m AVF (Fig. 6d). Such periods with persistent upward motion in the valley center were a quite regular feature in the late afternoon and early evening when the upvalley wind was established and were observed throughout the campaign. This is at odds with the classical "textbook" valley and slope wind circulation pattern according to Defant (1951).

At around 1900 LT, the time of the local sunset, a surface inversion started to form and the wind near the surface calmed down (Figs. 6a,b). Associated with the growing surface inversion, the upvalley wind layer gradually lifted and thinned. The upvalley wind slowly decreased in strength, but remained until after the end of the IOP at 0100 LT.

Spatial variability. To understand the observed vertical structure of the MoBL in the valley center and to capture the involved processes, additional spatial information is needed. Besides the observed down- and upvalley wind, thermally driven down- and upslope flows as well as dynamically induced circulations are expected to form, to interact with each other, and to impact the evolution of the MoBL.

In addition to the surface measurements at the i-Box flux towers, the PPI scans from the Streamline XR Doppler lidar are useful tools to provide information on the existence and variability of slope winds (Fig. 7). Between 0330 and 0400 LT (Figs. 7a,b), the i-Box towers

on the southern slopes reported downslope wind, while downvalley wind was detected at Eggen in the northern part of the valley, which is likely due to the location of the tower on the plateau. The PPI scan at a 4° elevation angle indicated that the downslope wind extended for some distance along the flat valley floor and superimposed on the downvalley wind (marked as "DS" in Fig. 7a). In the PPI scans at a 7° elevation angle, no downslope wind was visible (Fig. 7b). The distance between the laser beam and the underlying orography in the areas where the downslope wind was observed was less than 50 m at a 4° elevation angle and around 80–150 m at a 7° elevation angle. This indicates that the downslope wind layer was rather shallow (less than 80–150 m).

Upslope wind developed on the northern and southern slopes of the Inn Valley in the course of the day as detected by the i-Box towers (Figs. 7c,d). The upslope wind was visible in the PPI scans at a 4° elevation angle and also at a 7° elevation angle (marked as "US" in Figs. 7c,d), which indicates that the upslope wind layer had a vertical extent of more than 80 m (which is the approximate height of the laser beam at a 7° elevation angle above the orography in the areas where the upslope wind was detected). The upslope wind was more pronounced on the

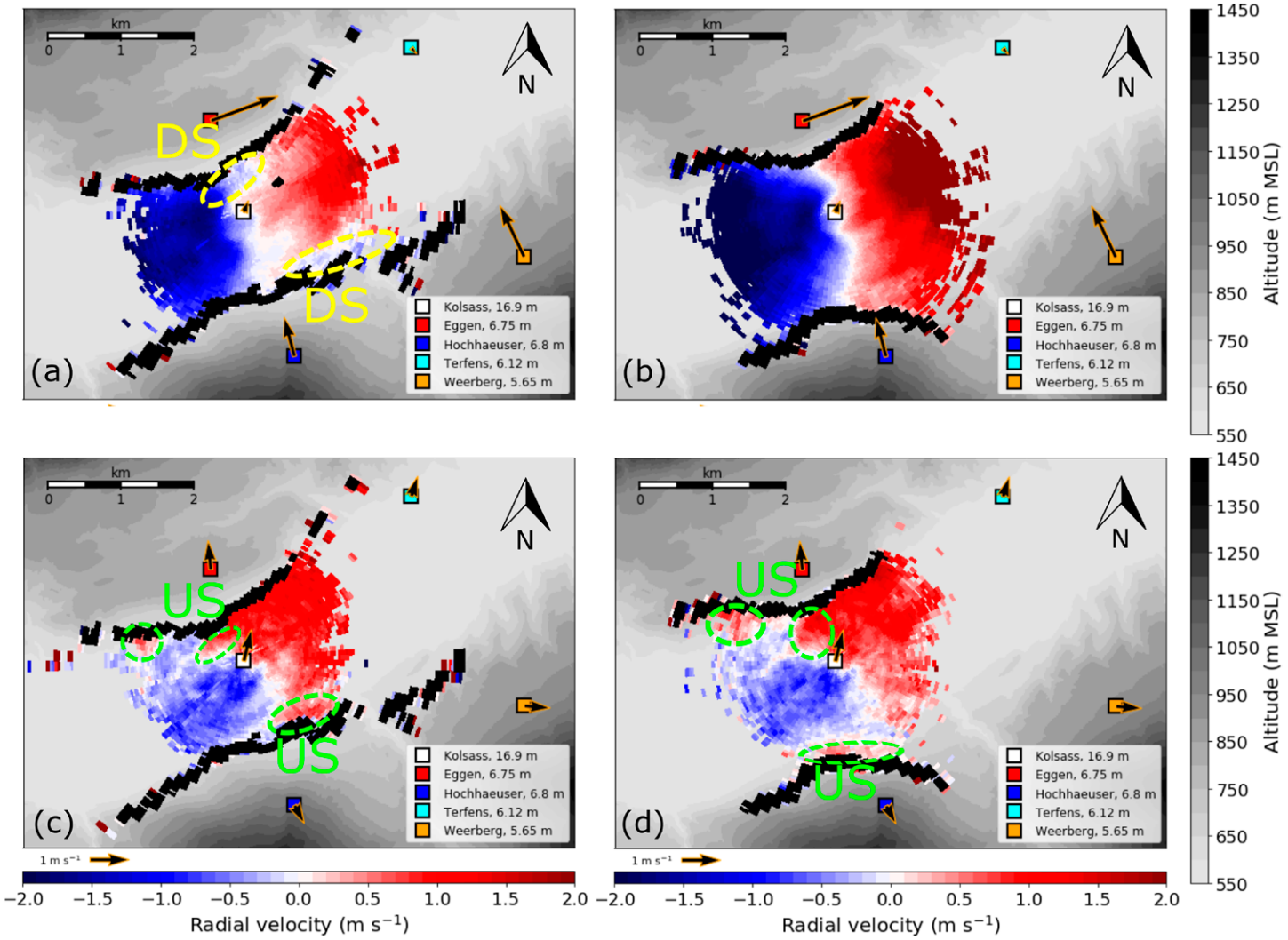

Fig. 7. Radial velocity from PPI scans at (a),(c) 4° and (b),(d) 7° elevation angle performed by the Streamline XR Doppler lidar at Kolsass and horizontal wind vectors (arrows) at five i-Box towers averaged for the period (a),(b) 0330–0400 LT and (c),(d) 1330–1400 LT during IOP 8 (13–14 Sep). A threshold for intensity (signal-to-noise ratio, SNR+1) of 1.005 and a jump filter of 2 m s^{-1} are applied to the radial velocity fields before averaging. Black pixels indicate range gates where the beam hits the topography (identified by a hard target filter). Negative (positive) radial velocity indicates flow toward (away from) the lidar. Areas with downslope (DS) and upslope (US) wind are indicated by the colored ovals.

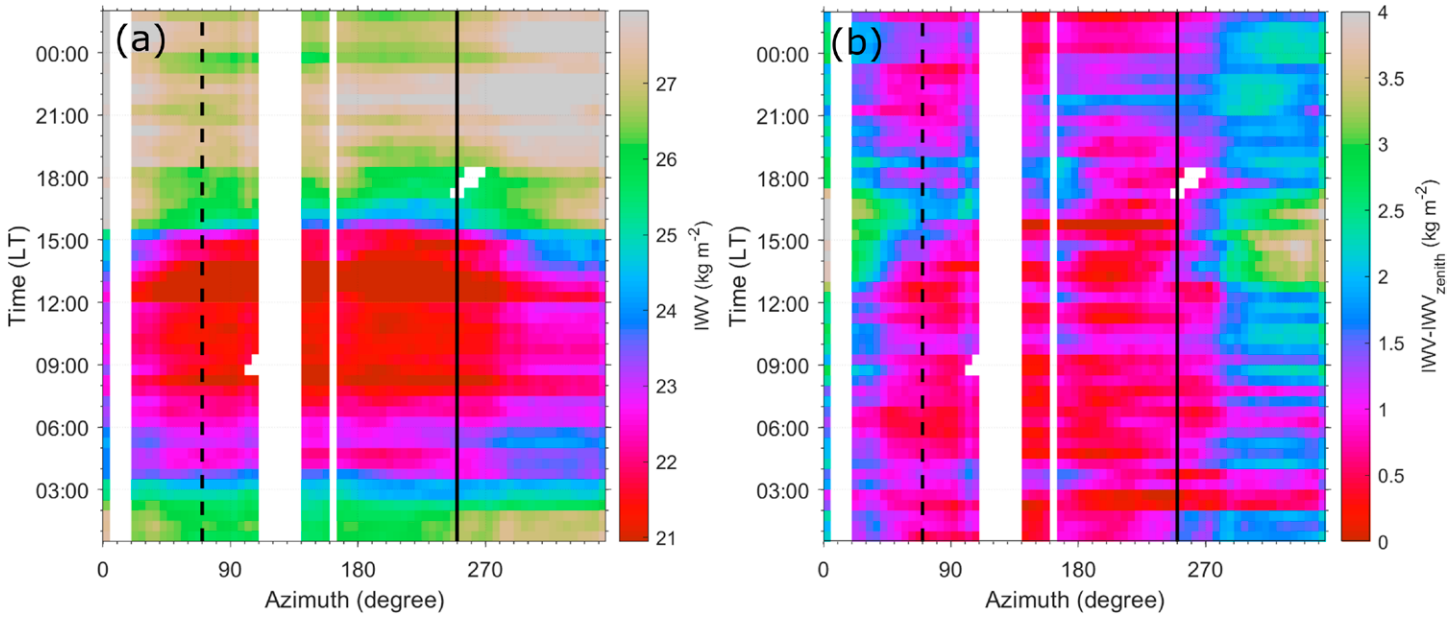

Fig. 8. Azimuthal time plot of (a) IWV at an elevation angle of 20.65° and (b) IWV at an elevation angle of 20.65° minus IWV at zenith retrieved from the HATPRO-G4 during IOP 8 (13–14 Sep). Missing values (white pixels) are caused by obstacles and sunrise or sunset. For better comparison with IWV measured at zenith, the values of the IWV from the PPI scans were normalized to a vertical column IWV = IWV$_{PPI}$sin(20.65°). Upvalley (dashed) and downvalley (solid) directions are indicated by the vertical black lines.

south-facing slope due to the stronger exposure to the sun. The upslope wind was particularly evident in the PPI scans when the along-valley wind component was weak, which was the case in the transition phase between downvalley and upvalley flow (Figs. 6a,b).

The radiosondes launched at Kolsass indicate that the stable valley atmosphere continuously dried throughout the morning due to the subsiding dry air mass and moistened only when the upvalley wind arrived (Fig. 6a). To obtain information on the spatial distribution of humidity in the valley and over the ridges, IWV from the half-hourly PPI scans performed by the HATPRO-G4 are a valuable indicator (Fig. 8). In particular over the northern ridge (about 280°–40°), the atmosphere was generally moister than in the valley center by more than 1 kg m^{-2} throughout the day. Between 1200 and 1330 LT, humidity increased by more than 2 kg m^{-2} over the northern ridge, while it still decreased in the valley center (about 190°–250° and 50°–100°). This indicates that moisture was transported upward over the ridge. Once the upvalley wind brought moister air into the valley (after 1530 LT, see also Fig. 6a), IWV increased in all directions (Fig. 8a). The spatial IWV difference between the valley center and the northern ridge, however, even increased to

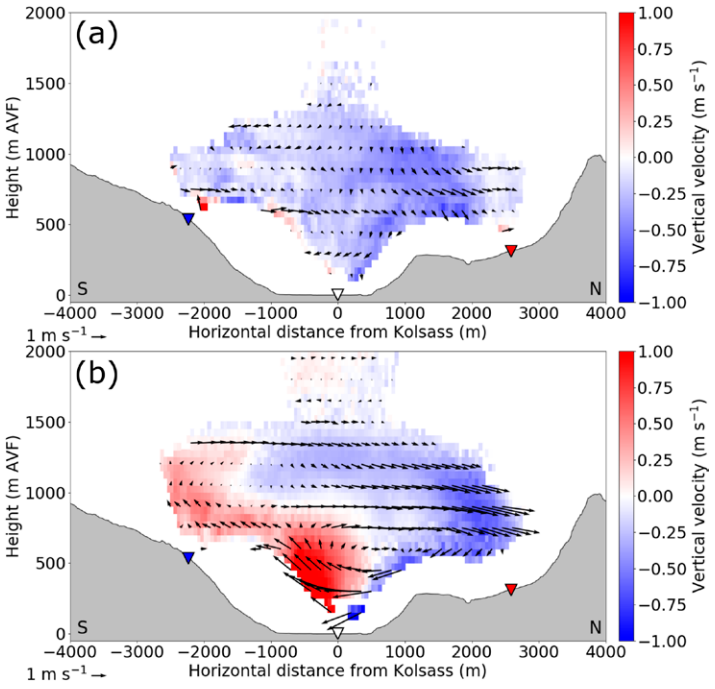

Fig. 9. Two-dimensional wind field (arrows) and vertical velocity (color-coded) retrieved from the coplanar Doppler lidar scans and averaged for the time periods (a) 1530–1615 and (b) 1700–1900 LT during IOP 8 (13–14 Sep). The markers indicate the locations of Hochhäuser (blue), Kolsass (white), and Mairbach (red).

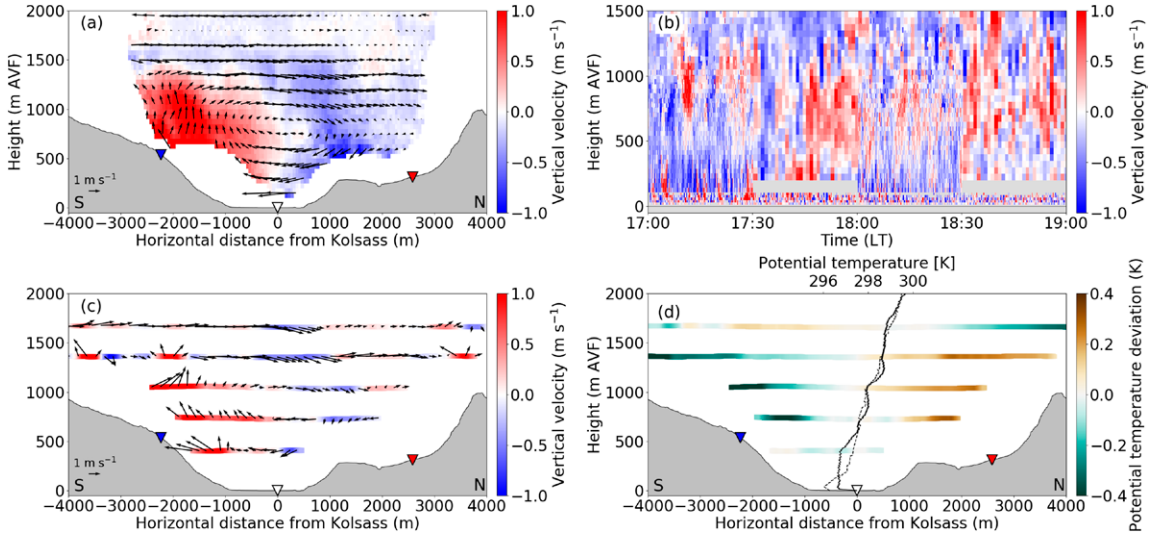

Fig. 10. Cross-valley circulation during IOP 4 (14–15 Aug): (a) two-dimensional wind field (arrows) and vertical velocity (color-coded) retrieved from the coplanar Doppler lidar scans and averaged for the time period 1800–1845 LT and (b) time–height section of vertical wind at Kolsass measured with the Windcube 200s, Streamline, and Wind Ranger Doppler lidars. The Wind Ranger measurements extend the data availability down to the surface. (c) Vertical velocity (color-coded) and two-dimensional wind vectors projected on the vertical plane (arrows) and (d) potential temperature deviation (color-coded, the reference is the value above Kolsass at each level) measured during the cross-valley aircraft flight between 1759 and 1817 LT. In (d), potential temperature profiles from the radio soundings at Kolsass at 1700 LT (solid line) and 1900 LT (dashed line) are shown. For better visibility, a moving average of 50 data points (approximately 325 m) is applied to all aircraft data in (c) and (d). The markers indicate the locations of Hochhäuser (blue), Kolsass (white), and Mairbach (red).

4 kg m $^{-2}$ in the afternoon and remained large until around 1700 LT (Fig. 8b).

The vertical velocity measured at Kolsass by the Doppler lidars revealed a period during the upvalley wind phase when subsidence dominated throughout the whole vertical measurement range (1530–1615 LT) and a period with strong and persistent upward motion (1700–1900 LT) (Fig. 6d). To investigate whether subsidence and upward motion were local phenomena or whether they occurred in a larger part of the valley and to understand the reason for them, the spatial flow structure has to be explored. To this purpose, we analyzed the two-dimensional wind field in the vertical plane across the valley retrieved from the coplanar Doppler lidar scans and averaged the wind field over the respective periods (Fig. 9). The mean subsidence during the first period clearly was not only local, but rather occurred in an area of several kilometers

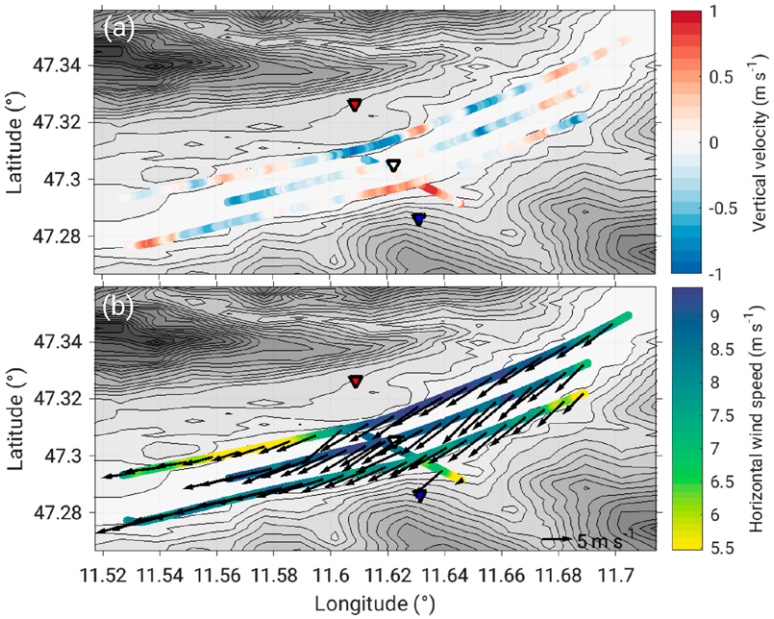

Fig. 11. (a) Vertical velocity and (b) horizontal wind speed (color-coded) and horizontal wind vectors (arrows) for along- and across-valley flight legs for the time period 1816–1833 LT during IOP 4 (14–15 Aug). Only legs between 252 and 446 m AVF are shown. For better visibility, a moving average of 50 data points (approximately 325 m) is applied. The markers indicate the locations of Mairbach (red), Kolsass (white), and Hochhäuser (blue).

across the valley and was strongest in the northern part (Fig. 9a). During the second period, the valley atmosphere can roughly be divided into two parts (Fig. 9b). In the northern part of the valley subsidence prevailed, while in the southern part and above Kolsass upward motion existed. Looking at the two-dimensional wind vector in the vertical plane, it is evident that a closed circulation cell existed in cross-valley direction, with a northerly component in the lower 700 m AVF and a southerly component above.

To understand the reason for this circulation, the along-valley dimension has to be considered, which is where the aircraft measurements come into play. As no aircraft flights were performed during IOP 8, we used the afternoon flight of IOP 4 during which a very similar persistent cross-valley circulation cell was detected in the wind field retrieved from the coplanar Doppler lidar scans (Fig. 10a). During IOP 4, the circulation cell had a larger vertical extent and the upward motion occurred predominantly in the southern part of the valley (Fig. 10a), leading to less pronounced upward motion above Kolsass (Fig. 10b) compared to IOP 8 (Figs. 6d and 9b). The simultaneously performed cross-valley flight legs nicely confirm this cross-valley circulation cell (Fig. 10c), even though the aircraft measurements are snapshots, while the lidar-retrieved wind field is a 45 min average. The potential temperature distribution was asymmetric with lower values in the southern and higher values in the northern part of the valley (Fig. 10d). The pattern with subsidence in the northern part of the valley and upward motion in the southern part can be observed in other sections of the valley as well (Fig. 11a). Taking into account the slight curvature of the valleys axis (to the right in upvalley direction), upward motion (Figs. 10a,c and 11a) and lower temperature (Fig. 10d) occurred in the outer part of the curve and the downward motion and higher temperature in the inner part. The upvalley wind prevailed in the whole valley, but showed a strong variability along and across the valley (Fig. 11b) with a deceleration toward the outer part of the curve east of Kolsass. This situation is different from the conditions observed in the Riviera Valley (Weigel and Rotach 2004). In a part of the Riviera Valley, where the valley axis curves to the left in upvalley direction, the along-valley wind component accelerated toward the outer part of the curve and downward motion in the outer part and upward motion in the inner part of the curve were found. While this is the opposite of what we observe in the Inn Valley, the tilt of the isentropes across the valley is the same in both valleys with colder air occurring in the outer part of the curve. The mechanism leading to this circulation in the Inn Valley remains to be investigated.

Summary and outlook

A meteorological field campaign was conducted in the Inn Valley in Austria from July to October 2019 to study the three-dimensional kinematic flow structure and its impact on the MoBL in the valley. To this purpose, the existing network of the i-Box surface flux towers and remote sensing instruments was expanded by additional continuously running remote sensing instruments and radio soundings and aircraft measurements were conducted during selected periods. This article describes the field campaign design and summarizes results of an initial analysis of the gathered data. The field campaign was designed (i) to monitor the vertical structure of the MoBL with high temporal resolution by continuously measuring wind, temperature, and humidity profiles in the valley center and (ii) to capture the spatial variability in the MoBL under different large-scale conditions. For the latter, the two-dimensional kinematic flow in a vertical plane across the valley was retrieved from continuous coplanar Doppler lidar scans, and in situ aircraft measurements of temperature, humidity, and wind were performed on stacked legs across and along the valley.

Thermally driven flows regularly developed in the Inn Valley during all IOPs. However, their strength, depth, and onset time varied considerably just like the large-scale wind speed and direction, cloud coverage and atmospheric stratification. During four IOPs, even

south foehn likely affected the conditions in the Inn Valley. The initial analysis clearly demonstrates that the combination of different sources of information allows to gain detailed insight into the spatial variability of the MoBL and to link the vertical MoBL structure to the three-dimensional flow. Some unexpected features were identified in the data, such as a single cross-valley circulation with upward motion in the outer part of the slightly curved valley. They will be the subject of subsequent detailed investigations. The gathered dataset is ideally suited for assessing the performance of mesoscale and large-eddy simulations with respect to cross-valley flow and is planned to be used for model evaluation in the future. As the MoBL depends on the energy input at the surface and on the large-scale conditions, its structure and evolution are likely different in valleys in, e.g., arid or tropical climates, and it would be interesting to investigate other valleys in the world with a similar experimental approach. Meteorological data from the CROSSINN field campaign are currently available from the authors on request and will be available to the public after the end of the project in 2022.

The instrument setup and measurement strategy of the CROSSINN field campaign will facilitate the planning and conduction of future campaigns, such as the upcoming large international program and experiment on multiscale transport and exchange processes over mountains (TEAMx; Rotach et al. 2020), the experimental part of which will partly take place in the Inn Valley. When planning to use Doppler lidars to observe the flow field in mountainous terrain, for example, the backscatter capability of the atmosphere has to be considered. It may be limited above mountain ridges or in regions with subsidence, e.g., in the valley center, due to the impact of dry, clean air from the free troposphere. The retrieval of the cross-valley flow in a vertical plane from coplanar Doppler lidar scans performed during CROSSINN is very promising and provides profound insights into the flow structure. During instrument setup and analysis, however, it has to be kept in mind that the retrieved two-dimensional wind components are a projection of the three-dimensional wind onto the vertical plane. The contribution of the valley wind or other large-scale influences to the retrieved two-dimensional wind field can only be estimated and depends on the strength and direction of the horizontal wind. As the vertical plane is determined by the physical locations of the lidars and cannot be changed depending on the wind direction, this contribution is unavoidable. The influence of the along-valley wind component, however, may be assessed when the spatial variability of the horizontal wind is known in detail. As the valley wind exhibits a large horizontal variability, measurements at single sites might not be representative. To avoid this, multiple profiling lidars could be distributed in the valley or—probably cheaper and more feasible—the virtual tower technique could be used to retrieve horizontal wind profiles at many arbitrary locations on the mesoscale (e.g., Calhoun et al. 2006; Wittkamp et al. 2021).

Acknowledgments. CROSSINN is funded by the Deutsche Forschungsgemeinschaft (DFG, German Research Foundation) under Grant 406279610. The DLR Cessna Grand Caravan 208 B flights were kindly financed by Karlsruhe Institute of Technology (KIT) and part of University of Innsbruck's contribution was financed through the research project PIANO funded by the Austrian Science Fund (FWF) and the Weiss Science Foundation under Grant P29746-N32. We thank all CROSSINN participants for their field and data processing assistance, including Karmen Babić, Shweta Singh, Timo Gamer, Martin Kohler, and Simone Scheer from KIT and Paul Ladstätter, Gaspard Simonet, Maximilian Stärz, Lukas Lehner, and Manuel Saigger from the University of Innsbruck. We are very grateful to Ludwig Wagner from GWU-Umwelttechnik GmbH for organizing the live test of the Raymetrics temperature lidar and to Hans-Jürgen Kirtzel from METEK for loaning the Wind Ranger lidar. We further thank the DLR aircraft team, including Marc Puskeiler, Frank Probst, Thomas van Marwick, Christian Mallaun, Vladyslav Nenakhov, Ralph Helmes, Stefan Hempe, and Georg Dietz. Special thanks go to Hubert Dengg in Hochhäuser and the owners of the riding stable Rantner in Mairbach for allowing the equipment to be installed on their grounds.

References

Adler, B., and N. Kalthoff, 2014: Multi-scale transport processes observed in the boundary layer over a mountainous island. *Bound.-Layer Meteor.*, **153**, 515–537, https://doi.org/10.1007/s10546-014-9957-8.

——, and ——, 2016: The impact of upstream flow on the atmospheric boundary layer in a valley on a mountainous island. *Bound.-Layer Meteor.*, **158**, 429–452, https://doi.org/10.1007/s10546-015-0092-y.

——, ——, and O. Kiseleva, 2020: Detection of structures in the horizontal wind field over complex terrain using coplanar Doppler lidar scans. *Meteor. Z.*, https://doi.org/10.1127/metz/2020/1031.

Baur, F., 2015: Determination of turbulent fluxes of airborne data in complex terrain using wavelet analysis. M.S. thesis, Dept. of Atmospheric and Cryospheric Sciences, University of Innsbruck, 139 pp., http://diglib.uibk.ac.at/urn:nbn:at:at-ubi:1-3205.

Bingöl, F., J. Mann, and D. Foussekis, 2009: Conically scanning lidar error in complex terrain. *Meteor. Z.*, **18**, 189–195, https://doi.org/10.1127/0941-2948/2009/0368.

Bougeault, P., and Coauthors, 2001: The MAP special observing period. *Bull. Amer. Meteor. Soc.*, **82**, 433–462, https://doi.org/10.1175/1520-0477(2001)082<0433:TMSOP>2.3.CO;2.

Brehm, M., 1982: Hangwindexperiment Innsbruck-Inversionsauflösung und Gebirgswindsystem. *Ann. Meteor.*, **19**, 150–152, http://nbn-resolving.de/urn:nbn:de:101:1-201708172379.

——, and C. Freytag, 1982: Erosion of the night-time thermal circulation in an Alpine valley. *Arch. Meteor. Geophys. Bioclimatol.*, **31B**, 331–352, https://doi.org/10.1007/BF02263439.

Browning, K., and R. Wexler, 1968: The determination of kinematic properties of a wind field using Doppler radar. *J. Appl. Meteor.*, **7**, 105–113, https://doi.org/10.1175/1520-0450(1968)007<0105:TDOKPO>2.0.CO;2.

Calhoun, R., R. Heap, M. Princevac, R. Newsom, H. Fernando, and D. Ligon, 2006: Virtual towers using coherent Doppler lidar during the Joint Urban 2003 dispersion experiment. *J. Appl. Meteor. Climatol.*, **45**, 1116–1126, https://doi.org/10.1175/JAM2391.1.

Crewell, S., and U. Löhnert, 2003: Accuracy of cloud liquid water path from ground-based microwave radiometry 2. sensor accuracy and synergy. *Radio Sci.*, **38**, 8042, https://doi.org/10.1029/2002RS002634.

——, and ——, 2007: Accuracy of boundary layer temperature profiles retrieved with multifrequency multiangle microwave radiometry. *IEEE Trans. Geosci. Remote Sens.*, **45**, 2195–2201, https://doi.org/10.1109/TGRS.2006.888434.

Defant, F., 1951: Local winds. *Compendium of Meteorology*, T. M. Malone, Ed., Amer. Meteor. Soc., 655–672, https://doi.org/10.1007/978-1-940033-70-9_54.

De Wekker, S. F., and M. Kossmann, 2015: Convective boundary layer heights over mountainous terrain – A review of concepts. *Front. Earth Sci.*, **3**, 77, https://doi.org/10.3389/feart.2015.00077.

Freytag, C., 1985: MERKUR-results: Aspects of the temperature field and the energy budget in a large Alpine valley during mountain and valley wind. *Contrib. Atmos. Phys.*, **58**, 458–476.

——, 1987: Results from the MERKUR experiment: Mass budget and vertical motions in a large valley during mountain and valley wind. *Meteor. Atmos. Phys.*, **37**, 129–140, https://doi.org/10.1007/BF01040843.

Goger, B., M. W. Rotach, A. Gohm, O. Fuhrer, I. Stiperski, and A. A. Holtslag, 2018: The impact of three-dimensional effects on the simulation of turbulence kinetic energy in a major Alpine valley. *Bound.-Layer Meteor.*, **168**, 1–27, https://doi.org/10.1007/s10546-018-0341-y.

——, ——, ——, I. Stiperski, O. Fuhrer, and G. De Morsier, 2019: A new horizontal length scale for a three-dimensional turbulence parameterization in mesoscale atmospheric modeling over highly complex terrain. *J. Appl. Meteor. Climatol.*, **58**, 2087–2102, https://doi.org/10.1175/JAMC-D-18-0328.1.

Gohm, A., G. Zängl, and G. J. Mayr, 2004: South foehn in the Wipp Valley on 24 October 1999 (MAP IOP 10): Verification of high-resolution numerical simulations with observations. *Mon. Wea. Rev.*, **132**, 78–102, https://doi.org/10.1175/1520-0493(2004)132<0078:SFITWV>2.0.CO;2.

——, and Coauthors, 2009: Air pollution transport in an Alpine valley: Results from airborne and ground-based observations. *Bound.-Layer Meteor.*, **131**, 441–463, https://doi.org/10.1007/s10546-009-9371-9.

Haid, M., 2019: Marenha/doppler_wind_lidar_toolbox: First release (v1.0.0). Zenodo, https://doi.org/10.5281/zenodo.3583083.

——, A. Gohm, L. Umek, H. C. Ward, T. Muschinski, L. Lehner, and M. W. Rotach, 2020: Foehn-cold pool interactions in the Inn Valley during PIANO IOP2. *Quart. J. Roy. Meteor. Soc.*, **146**, 1232–1263, https://doi.org/10.1002/qj.3735.

Harnisch, F., A. Gohm, A. Fix, R. Schnitzhofer, A. Hansel, and B. Neininger, 2009: Spatial distribution of aerosols in the Inn Valley atmosphere during wintertime. *Meteor. Atmos. Phys.*, **103**, 223–235, https://doi.org/10.1007/s00703-008-0318-3.

Hill, M., R. Calhoun, H. Fernando, A. Wieser, A. Dörnbrack, M. Weissmann, G. Mayr, and R. Newsom, 2010: Coplanar Doppler lidar retrieval of rotors from T-REX. *J. Atmos. Sci.*, **67**, 713–729, https://doi.org/10.1175/2009JAS3016.1.

Jackson, P. L., G. Mayr, and S. Vosper, 2013: Dynamically-driven winds. *Mountain Weather Research and Forecasting*, F. K. Chow, S. F. De Wekker, and B. J. Snyder, Eds., Springer, 121–218, https://doi.org/10.1007/978-94-007-4098-3_3.

Kalthoff, N., and Coauthors, 2013: KITcube – A mobile observation platform for convection studies deployed during HyMeX. *Meteor. Z.*, **22**, 633–647, https://doi.org/10.1127/0941-2948/2013/0542.

Karl, T., and Coauthors, 2020: Studying urban climate and air quality in the Alps: The Innsbruck Atmospheric Observatory. *Bull. Amer. Meteor. Soc.*, **101**, E488–E507, https://doi.org/10.1175/BAMS-D-19-0270.1.

Kirshbaum, D. J., B. Adler, N. Kalthoff, C. Barthlott, and S. Serafin, 2018: Moist orographic convection: Physical mechanisms and links to surface-exchange processes. *Atmosphere*, **9**, 80, https://doi.org/10.3390/atmos9030080.

Kuettner, J. P., and T. H. O'Neill, 1981: ALPEX the GARP mountain subprogram. *Bull. Amer. Meteor. Soc.*, **62**, 793–805, https://doi.org/10.1175/1520-0477-62.6.793.

Lehner, M., and M. W. Rotach, 2018: Current challenges in understanding and predicting transport and exchange in the atmosphere over mountainous terrain. *Atmosphere*, **9**, 276, https://doi.org/10.3390/atmos9070276.

——, ——, and F. Obleitner, 2019: A method to identify synoptically undisturbed, clear-sky conditions for valley-wind analysis. *Bound.-Layer Meteor.*, **173**, 435–450, https://doi.org/10.1007/s10546-019-00471-2.

Leukauf, D., A. Gohm, and M. W. Rotach, 2017: Toward generalizing the impact of surface heating, stratification and terrain geometry on the daytime heat export from an idealized valley. *J. Appl. Meteor. Climatol.*, **56**, 2711–2727, https://doi.org/10.1175/JAMC-D-16-0378.1.

Löhnert, U., D. Turner, and S. Crewell, 2009: Ground-based temperature and humidity profiling using spectral infrared and microwave observations. Part I: Simulated retrieval performance in clear-sky conditions. *J. Appl. Meteor. Climatol.*, **48**, 1017–1032, https://doi.org/10.1175/2008JAMC2060.1.

Mallaun, C., A. Giez, and R. Baumann, 2015: Calibration of 3-D wind measurements on a single-engine research aircraft. *Atmos. Meas. Tech.*, **8**, 3177–3196, https://doi.org/10.5194/amt-8-3177-2015.

Massaro, G., I. Stiperski, B. Pospichal, and M. W. Rotach, 2015: Accuracy of retrieving temperature and humidity profiles by ground-based microwave radiometry in truly complex terrain. *Atmos. Meas. Tech.*, **8**, 3355–3367, https://doi.org/10.5194/amt-8-3355-2015.

Muschinski, T., A. Gohm, M. Haid, L. Umek, and H. C. Ward, 2021: Spatial heterogeneity of the Inn Valley cold air pool during south foehn: Observations from an array of temperature loggers during PIANO. *Meteor. Z.*, https://doi.org/10.1127/metz/2020/1043, in press.

Newsom, R., R. Calhoun, D. Ligon, and J. Allwine, 2008: Linearly organized turbulence structures observed over a suburban area by dual-Doppler lidar. *Bound.-Layer Meteor.*, **127**, 111–130, https://doi.org/10.1007/s10546-007-9243-0.

Peters, G., 2018: Reliable data - continuous wave lidars can provide more accurate wind measurements with high resolution at short distances. *Meteorological*

Technology International, September issue, 106–108, www.ukimediaevents.com/publication/8511a42f/1.

Plavcan, D., G. J. Mayr, and A. Zeileis, 2014: Automatic and probabilistic foehn diagnosis with a statistical mixture model. *J. Appl. Meteor. Climatol.*, **53**, 652–659, https://doi.org/10.1175/JAMC-D-13-0267.1.

Reichardt, J., U. Wandinger, V. Klein, I. Mattis, B. Hilber, and R. Begbie, 2012: RAMSES: German Meteorological Service autonomous Raman lidar for water vapor, temperature, aerosol, and cloud measurements. *Appl. Opt.*, **51**, 8111–8131, https://doi.org/10.1364/AO.51.008111.

Rotach, M. W., and D. Zardi, 2007: On the boundary-layer structure over highly complex terrain: Key findings from MAP. *Quart. J. Roy. Meteor. Soc.*, **133**, 937–948, https://doi.org/10.1002/QJ.71.

——, G. Wohlfahrt, A. Hansel, M. Reif, J. Wagner, and A. Gohm, 2014: The world is not flat: Implications for the global carbon balance. *Bull. Amer. Meteor. Soc.*, **95**, 1021–1028, https://doi.org/10.1175/BAMS-D-13-00109.1.

——, and Coauthors, 2017: Investigating exchange processes over complex topography: The Innsbruck Box (i-Box). *Bull. Amer. Meteor. Soc.*, **98**, 787–805, https://doi.org/10.1175/BAMS-D-15-00246.1.

——, and Coauthors, 2020: *Multi-Scale Transport and Exchange Processes in the Atmosphere Over Mountains*. Innsbruck University Press, 42 pp., https://doi.org/10.15203/99106-003-1.

Rucker, M., R. M. Banta, and D. G. Steyn, 2008: Along-valley structure of daytime thermally driven flows in the Wipp Valley. *J. Appl. Meteor. Climatol.*, **47**, 733–751, https://doi.org/10.1175/2007JAMC1319.1.

Schmidli, J., 2013: Daytime heat transfer processes over mountainous terrain. *J. Atmos. Sci.*, **70**, 4041–4066, https://doi.org/10.1175/JAS-D-13-083.1.

Schnitzhofer, R., and Coauthors, 2009: A multimethodological approach to study the spatial distribution of air pollution in an Alpine valley during wintertime. *Atmos. Chem. Phys.*, **9**, 3385–3396, https://doi.org/10.5194/acpd-9-3983-2009.

Serafin, S., and D. Zardi, 2010: Daytime heat transfer processes related to slope flows and turbulent convection in an idealized mountain valley. *J. Atmos. Sci.*, **67**, 3739–3756, https://doi.org/10.1175/2010JAS3428.1.

——, L. Strauss, and V. Grubišić, 2017: Climatology of westerly wind events in the lee of the Sierra Nevada. *J. Appl. Meteor. Climatol.*, **56**, 1003–1023, https://doi.org/10.1175/JAMC-D-16-0244.1.

——, and Coauthors, 2018: Exchange processes in the atmospheric boundary layer over mountainous terrain. *Atmosphere*, **9**, 102, https://doi.org/10.3390/atmos9030102.

Sfyri, E., M. W. Rotach, I. Stiperski, F. C. Bosveld, M. Lehner, and F. Obleitner, 2018: Scalar-flux similarity in the layer near the surface over mountainous terrain. *Bound.-Layer Meteor.*, **169**, 11–46, https://doi.org/10.1007/s10546-018-0365-3.

Stawiarski, C., K. Träumner, C. Knigge, and R. Calhoun, 2013: Scopes and challenges of dual-Doppler lidar wind measurements—An error analysis. *J. Atmos. Oceanic Technol.*, **30**, 2044–2062, https://doi.org/10.1175/JTECH-D-12-00244.1.

Steyn, D. G., S. F. J. De Wekker, M. Kossmann, and A. Martilli, 2013: Boundary layers and air quality in mountainous terrain. *Mountain Weather Research and Forecasting*, F. K. Chow, S. F. De Wekker, and B. J. Snyder, Eds., Springer, 261–289, https://doi.org/10.1007/978-94-007-4098-3_5.

Stiperski, I., and M. W. Rotach, 2016: On the measurement of turbulence over complex mountainous terrain. *Bound.-Layer Meteor.*, **159**, 97–121, https://doi.org/10.1007/s10546-015-0103-z.

——, M. Calaf, and M. W. Rotach, 2019: Scaling, anisotropy, and complexity in near-surface atmospheric turbulence. *J. Geophys. Res. Atmos.*, **124**, 1428–1448, https://doi.org/10.1029/2018JD029383.

Strauss, L., S. Serafin, and V. Grubišić, 2016: Atmospheric rotors and severe turbulence in a long deep valley. *J. Atmos. Sci.*, **73**, 1481–1506, https://doi.org/10.1175/JAS-D-15-0192.1.

Träumner, K., T. Damian, C. Stawiarski, and A. Wieser, 2015: Turbulent structures and coherence in the atmospheric surface layer. *Bound.-Layer Meteor.*, **154**, 1–25, https://doi.org/10.1007/s10546-014-9967-6.

Vergeiner, I., 1982: Eine energetische Theorie der Hangwinde. *Ann. Meteor.*, **19**, 189–191, http://nbn-resolving.de/urn:nbn:de:101:1-201708172379.

——, and E. Dreiseitl, 1987: Valley winds and slope winds—Observations and elementary thoughts. *Meteor. Atmos. Phys.*, **36**, 264–286, https://doi.org/10.1007/BF01045154.

Wagner, J., A. Gohm, and M. Rotach, 2015: The impact of valley geometry on daytime thermally driven flows and vertical transport processes. *Quart. J. Roy. Meteor. Soc.*, **141**, 1780–1794, https://doi.org/10.1002/qj.2481.

Weigel, A. P., and M. W. Rotach, 2004: Flow structure and turbulence characteristics of the daytime atmosphere in a steep and narrow Alpine valley. *Quart. J. Roy. Meteor. Soc.*, **130**, 2605–2627, https://doi.org/10.1256/qj.03.214.

Whiteman, C. D., and Coauthors, 2018: The nocturnal evolution of atmospheric structure in a basin as a larger-scale katabatic flow is lifted over its rim. *J. Appl. Meteor. Climatol.*, **57**, 969–989, https://doi.org/10.1175/JAMC-D-17-0156.1.

Wildmann, N., S. Kigle, and T. Gerz, 2018: Coplanar lidar measurement of a single wind energy converter wake in distinct atmospheric stability regimes at the Perdigão 2017 experiment. *J. Phys.: Conf. Ser.*, **1037**, 052006, https://doi.org/10.1088/1742-6596/1037/5/052006.

Wittkamp, N., B. Adler, N. Kalthoff, and O. Kiseleva, 2021: Mesoscale wind patterns over the complex urban terrain around Stuttgart investigated with dual-Doppler lidar profiles. *Meteor. Z.*, https://doi.org/10.1127/metz/2020/1029, in press.

Zängl, G., 2004: A reexamination of the valley wind system in the Alpine Inn Valley with numerical simulations. *Meteor. Atmos. Phys.*, **87**, 241–256, https://doi.org/10.1007/s00703-003-0056-5.

——, 2009: The impact of weak synoptic forcing on the valley-wind circulation in the Alpine Inn Valley. *Meteor. Atmos. Phys.*, **105**, 37–53, https://doi.org/10.1007/s00703-009-0030-y.

Zardi, D., and C. D. Whiteman, 2013: Diurnal mountain wind systems. *Mountain Weather Research and Forecasting*, F. K. Chow, S. F. J. De Wekker, and B. J. Snyder, Eds., Springer, 35–119, https://doi.org/10.1007/978-94-007-4098-3_2.